Starch modified hyperbranched polyurethane/reduced carbon dot nanocomposite

Highlight

Current chapter deals with the fabrication of potential smart suture from reduced carbon dot (RCD) based starch modified hyperbranched polyurethane (HPU) nanocomposite with potent biocompatibility and high performance. The chapter is divided into two sub-chapters, where **Sub-Chapter 4A** depicts the synthesis, characterization and property assessment of bio-based luminescent RCD nanomaterial. **Sub-Chapter 4B** deals with the *in situ* fabrication of high performance starch modified HPU nanocomposites with different weight percentages of RCD. The desired mechanical and thermal attributes of the nanocomposites were achieved with 2 wt% of RCD in the HPU matrix. Non-contact self tightening behavior of the nanocomposites was observed at body temperature (37 ± 1) °C with notable shape fixity and shape recovery effects. Low lactate dehydrogenase activity and minimal RBC lysis indicated the anti-thrombogenicity and anti-hemolytic properties of the nanocomposites. The nanocomposites displayed inherent biocompatibility as observed by the growth and proliferation of smooth muscle cells and endothelial cells. Thus, the study paved the way to biodegradable HPU nanocomposites as advanced non-contact triggered rapid self tightening surgical sutures for biomedical applications.

Parts of this work are published in

[1] **Duarah, R.** and Karak, N. Facile and ultrafast green approach to synthesize biobased luminescent reduced carbon nanodot: an efficient photocatalyst. *ACS Sustainable Chemistry & Engineering,* 5**:**9454-9466, 2017.

[2] **Duarah, R.**, Singh Y. P., Gupta, P., Mandal, B. B., and Karak, N. High performance bio-based hyperbranched polyurethane/carbon dot silver nanocomposite: a rapid self-expandable stent. *Biofabrication,* 8:045013, 2016.

4A. Bio-based luminescent reduced carbon nanodot

4A.1. Introduction

The previous chapter discussed the development of a biocompatible, antibacterial and tough starch modified hyperbranched polyurethane/carbon dot-silver (HPU/CD-Ag) nanocomposite as a potential self-expandable stent for endoscopic surgeries. Yet, the enhancement of attributes such as shape memory, toughness and elongation at break are not very significant for advanced biomedical applications. This may be due to the presence of huge amount of functionality on carbon dot (CD) which causes difficulties in the fabrication process and chance of aggregation of nanomaterial. In this milieu, reduced CD (RCD) with optimum functionality may be an apt option. Further, such nanomaterials can be obtained by a facile hydrothermal approach using aqueous phytoextracts. The incorporation of such carbon based nanomaterial into a shape memory polymer(s) (SMP) may result in a mechanically strong, sustainable and biocompatible material. This is possible because of the fact that RCD has graphitic structure and the optimum polar peripheral groups of it may confer a strong physicochemical interaction with the similar polar functional group containing hyperbranched polyurethane (HPU) matrix.

Previous literature cites the use of several conventional reductants such as ascorbic acid, sodium sulfide, sodium citrate, sodium borohydride, hydrazine hydrate, etc. to reduce CD without significant increase in the luminescence or emission shift [1-3]. Further, such chemical routes are unfavorable due to environmental issues [4]. In contrast, no report is found on reduction of CD by using naturally renewable low cost, non toxic reducing agent such as phytoextracts which contain different polyphenolic compounds with high reducing ability. Therefore, RCD from bio-based precursors by using *Calocasia esculenta* (*C. esculenta*) leaf extract by a simple facile one-step green approach was developed for the first time. The developed RCD by virtue of attributes like bio-based origin, profound bio-activity and no volatile organic compounds (VOC) content has the prospective to address a cocktail of challenges ranging from sustainability to environmental footprints. Most significantly this RCD possesses a higher degree of sustainability over a purely chemical route.

Again, the unique structure and PL properties (strong visible to NIR light absorption capacity with enhanced fluorescence) of RCD may open a host of additional possibilities such as its efficient use as a photocatalyst for degradation of organic contaminant(s) (OC) [5, 6]. Among the different hazardous anthropogenic organic chemicals, bisphenol A [2, 2-bis (4-hydroxyphenyl) propane, BPA] is a non-degradable chemical contaminant, both in water and the soil causing endocrine disruption [7, 8]. Thus, scientists have developed effective remediation technologies for the destruction of BPA in water, including ultrasonic, Fenton oxidation, H_2O_2 oxidation and photocatalytic methods [9]. However, the degradation of BPA by a nano photocatalyst is limited, and the efficiency of such reported catalysts is significantly very poor even under UV irradiation [7-9]. In this context, the synthesized RCD with improved photocatalytic activity under sunlight may efficiently degrade BPA.

Thus, the well characterized sustainable resource-based this luminescent RCD was attempted to use as an efficient photocatalyst for degradation of organic pollutants like toxic BPA, methylene blue (MB), methyl orange (MO) and methylene blue/methyl orange (MB/MO) mixture under normal sunlight. Thus, in the present sub-chapter, a sustainable, efficient and harmless approach for the synthesis of bio-based RCD by reducing starch based CD using aqueous phytoextracts, was developed.

4A.2. Experimental

4A.2.1. Materials

Starch and BPA employed, were of similar grade and specifications as described in **Chapter 2**. *Citrus limon* (*C. limon*) fruits and *Syzygium aromaticum* (*S. aromaticum*) flower buds were purchased from the local market at Tezpur, India. *C. esculenta*, *Mesua ferrea Linn. (M. ferrea Linn.*) and tea leaves were collected from local area.

4A.2.2. Phytoextract preparation

About 2 g of *C. esculenta*, *M. ferrea Linn.* or tea leaves; or *S. aromaticum* flower buds was washed separately with water and coarsely grounded using a domestic blender followed by stirring for about 30 min in 50 mL of water at 60 °C. The aqueous extract was filtered under ambient conditions.

4A.2.3. RCD synthesis

At first CD was synthesized by a facile green one-step hydrothermal synthetic route using starch and *C. limon* extract, without base, as reported in **Chapter 3** (**Section 3.2.3.1**). Subsequently, RCD was synthesized by reducing CD via a single step green facile process using various phytoextracts. In a typical process, 10 mL of aqueous extract of *C. esculenta* leaf and Fe^{3+} ions (10 mL of 0.01 M) were slowly added drop wise to 100 mg of CD solution at room temperature under continuous stirring. Other aqueous phytoextracts like *M. Ferrea Linn*. leaf, tea leaf and *S. aromacticum* flower bud with Fe^{3+} ions as well as *C. esculenta* with other metal ions Cu^{2+}, Ni^{2+} and Cr^{2+} ions were also used separately for the reduction of CD under the same conditions. The change of color from light brown was taken as completion of the reduction process and was supported by UV analysis. The product was washed thrice with ultrapure water and isolated by centrifuging at 8000 rpm for 10 min. This process removed water soluble components and finally the residue was redispersed in water by ultrasonication. The preparation of RCD was also carried out under refluxed condition using the same technique and reducing agents for comparison purposes.

4A.2.4. Characterization

RCD was characterized by Fourier Transformed Infrared (FTIR), X-ray diffraction (XRD), Raman, UV-visible, High Resolution Transmission Electron Microscopic (HRTEM), Electron Dispersive X-ray (EDX) and thermogravimetric analysis (TGA) under the same conditions using the same instruments as stated in **Chapter 2** (**Section 2.2.2**). The photoluminescent spectra were taken by a photoluminescent setup (Perkin Elemer Singapore PTE Ltd., Singapore, Model LS 55) in aqueous solution. The quantum yields of CD and RCD were calculated using quinine sulphate as the reference. CD and RCD were dispersed in water while quinine sulphate was dissolved in 0.1 M H_2SO_4. Their fluorescence spectra were recorded by fluorescence spectrophotometer at excitation wavelengths 300, 320, 340, 360, 380 and 400 nm. The quantum yields of CD and RCD were subsequently determined by comparing the integrated photoluminescence intensities (excited at 340 nm and 360 nm) and the absorbance value (at the mentioned wavelengths) of CD and RCD with the reference quinine sulphate. The absorbance values of the solutions at the excitation wavelength were measured by an UV-vis spectrophotometer. Quantum yield was calculated by using the formula as given below.

$$(Q)_{RCD} = (Q)_{RCD}.I_{RCD}/I_R.A_R/A_{RCD}.(\eta_{RCD})^2/(\eta_R)^2 \ldots\ldots\ldots\ldots\ldots\ldots\ldots\ldots\ldots \quad \textbf{(Eq. 4A.1)}$$

Where ‘Q’ refers to the quantum yield, ‘I’ refers to the intensity of fluorescence, ‘A’ is the absorbance at excited wavelength and ‘η’ is the refractive index of the solvent used. The subscripts ‘RCD’ and ‘R’ used in the equation refer to reduced carbon dot and reference (quinine sulphate), respectively. The electrical conductivity of CD and RCD pellets of 1 cm diameter was measured by using a Keithley 2400 C source meter (Tanotis, India)

4A.2.5. Photocatalytic activity

Organic dyes like MB, MO, MB/MO mixture and organic pollutants like BPA were used for the determination of photocatalytic degradation activity of RCD and CD. In a typical procedure, 50 mg of RCD was taken in four separate flasks containing 100 mL aqueous solution of MB (10 mg L^{-1}), MO (10 mg L^{-1}), MB/MO mixture (10 mg L^{-1} each, separately) and BPA (50 mg L^{-1}). The solutions were stirred under normal solar light (60000-80000 lux) at room temperature. The experiment was also done using same amount of CD for comparison purpose. The change in concentration of MB, MO and BPA was monitored by determining UV absorbance intensity at wavelengths of 657 nm, 459 nm and 273 nm, respectively under specified time intervals [7, 10]. The activity of the catalyst was calculated from the rate of change of concentration of the dye. The same experiment was also conducted using same amount of CD for comparison purpose. The amount of the degraded pollutants was obtained by using the following equation.

$$\text{Degradation (\%)} = [(C_0-C)/C_0 \times 100] \qquad \textbf{(Eq. 4A.2)}$$

Where C_0 is the initial concentration and C is the concentration after photocatalytic degradation of the pollutant.

4A.3. Results and discussion

4A.3.1. Synthesis and characterization of RCD

CD was synthesized by hydrothermal acid hydrolysis of the aqueous ethanolic solution of starch and citric acid as the bio-based carbon precursors using the same method as described in **Chapter 3** (**Section 3.2.3.1**). The times required for catalytic reduction of CD under reflux conditions as well as at room temperature by different phytoextracts, are given in **Table 4A.1**.

Table 4A.1. Time taken (h) by different phytoextracts for reduction of CD

Phytoextract	Room temperature	Refluxed condition
C. esculenta	3	1
M. ferrea Linn.	4	2
Tea	5	2.5
S. aromaticum	6	3.5

The results showed that reduction was fastest in case of *C. esculenta* leaf extract among the used phytochemicals. Further, the reduction was much faster under refluxed condition than at room temperature in all the cases, as the activation energy for reduction was achieved at a faster rate at higher temperature. It was also observed that the amount of phytoextract did not affect the time for reduction. Further, the reduction of CD by aqueous phytoextract in the presence of different metal ions (Fe^{3+}, Cu^{2+}, Ni^{2+} and Cr^{2+} ions) under ambient condition revealed the effective reduction only with Fe^{3+} ions [11]. The reduction times for different phytoextracts in the presence of Fe^{3+} ions, with and without sonication clearly demonstrated the efficiency of *C. esculenta* leaf extract, as shown in **Table 4A.2**.

Table 4A.2. Time taken (min) by different phytoextracts in the presence of Fe^{3+} ions for reduction of CD with and without sonication

Phytoextract + Fe^{3+} ions	With sonication	Without sonication
C. esculenta	3	10
M. ferrea Linn.	5	20
Tea	10	25
S. aromaticum	10	30

It took only 3 min with sonication whereas 10 min was required without sonication. This is a significant achievement as the reduction time was drastically reduced by this approach. This may be due to complex formation between Fe^{3+} and the polyphenol groups of the phytoextract as supported by UV-visible absorbance data [4, 12]. The schematic representation of the synthesis of RCD using *C. esculenta* leaf extract in presence of Fe^{3+} ions is shown in **Scheme 4A.1**. Literature cites *C. esculenta* leaf extract contains polyphenolic compounds like pectins, flavonoids, ascorbic acid, apigenin, luteolin, and various flavones which showed strong potential for reduction of graphene oxide (GO) as reported earlier [4, 13]. The reduction potential of this phytoextract was also reported to be enhanced by addition of Fe^{3+} ions [14]. These polyphenolic compounds contain different polar functional groups such as hydroxyl, carboxy etc. which can form complexes with Fe^{3+} ions [4, 12].

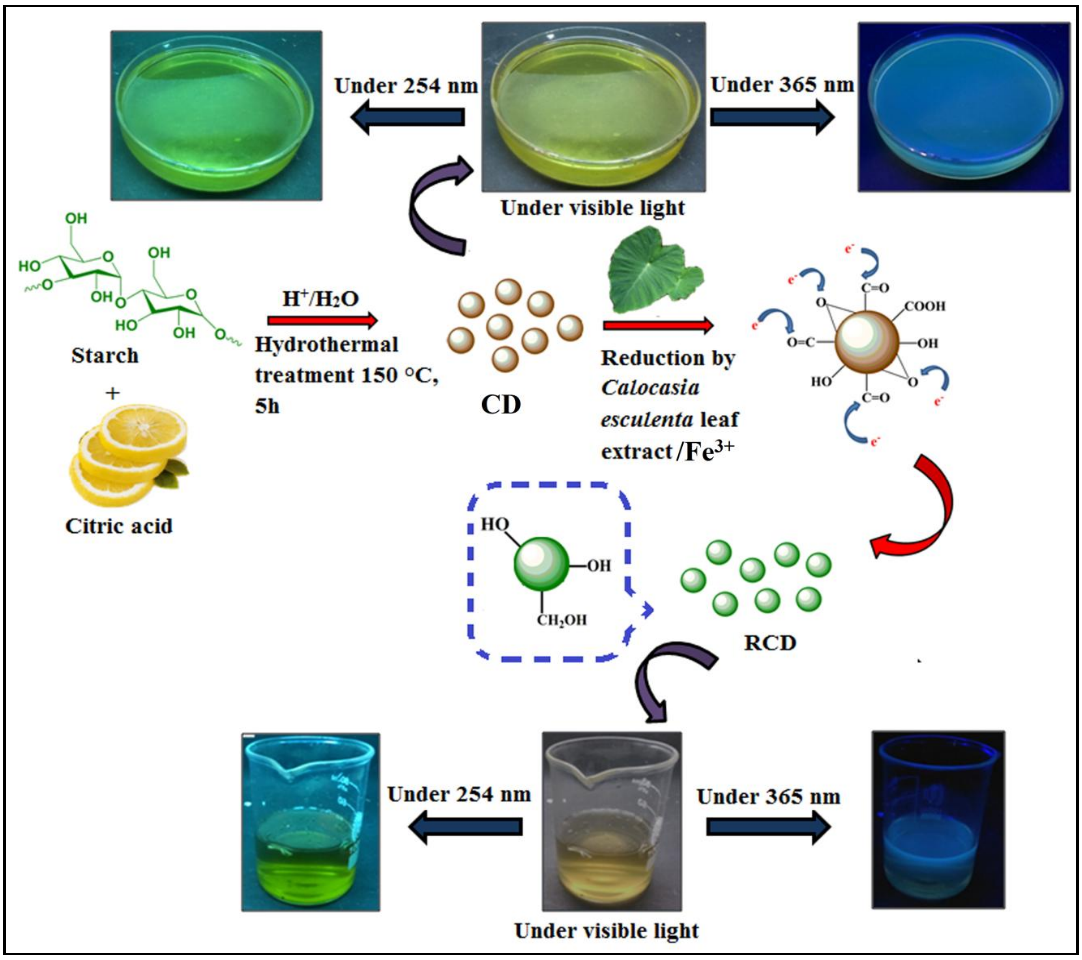

Scheme 4A.1. Synthesis of RCD by *C. esculenta* leaf extract in presence of Fe^{3+} ions.

The absorption at 277 nm may be due to the formation of such complexes as depicted in the given reaction [11].

$$6ArOH + FeCl_3 \longrightarrow H_3[Fe(OAr)_6] + 3HCl \;\ldots\ldots\ldots\ldots\ldots\ldots\ldots \textbf{(Eq. 4A.3)}$$

Iron polyphenolic complex

The time for reduction was dependent on the rate of complex formation, as Fe^{3+} ions might form a more stable and stronger complex with polyphenol, present in the extract compared to other metal ions, and thereby exhibiting faster reduction.

The plausible mechanism for transfer of electron(s) (e^-) for the reduction of CD is shown in **Scheme 4A.2** where reduction was achieved by e^- transfer as well as nucleophilic attack (S_N^2) mechanism. During the complexation, high amount of H^+ ions was released, which changes the pH of the system [12]. The pH of phytoextract and metal ion containing *C. esculenta* leaf extract were measured to be around 6 and 3, respectively.

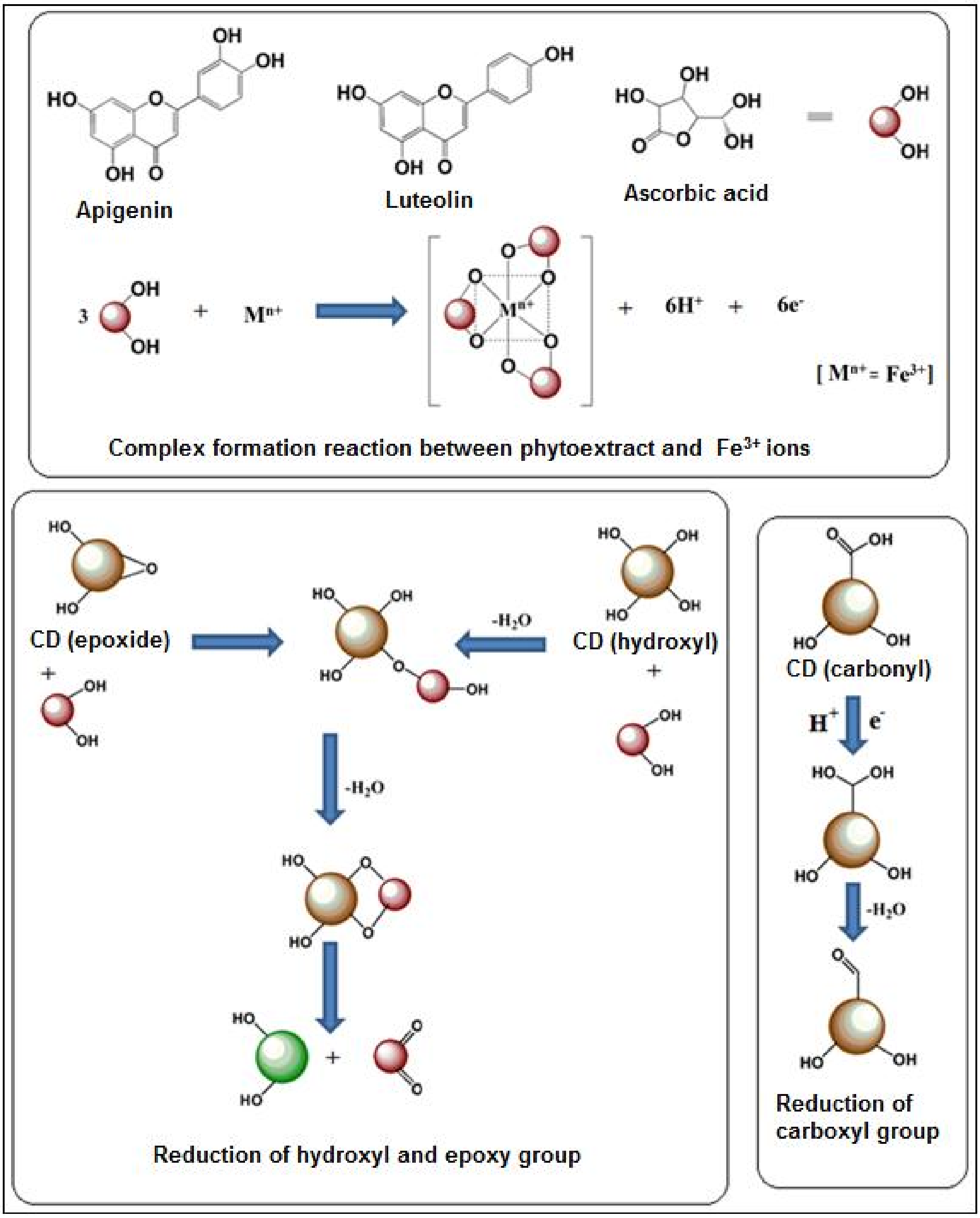

Scheme 4A.2. Plausible electron transfer mechanism for the reduction of CD.

For the better understanding of the result of pH, reduction was also carried out by adjusting the pH of the mixed suspension at 3. But even after 1 h, no effective reduction was achieved which implies that pH has no influence in the course of reduction. After complete reduction, a red shift of characteristic peak was observed at 269 nm, in the UV-visible spectrum of RCD, which indicates that electronic conjugation was restored [12, 15]. Further, the optical absorption of RCD was found to be higher than that of CD (**Figure 4A.1a**).

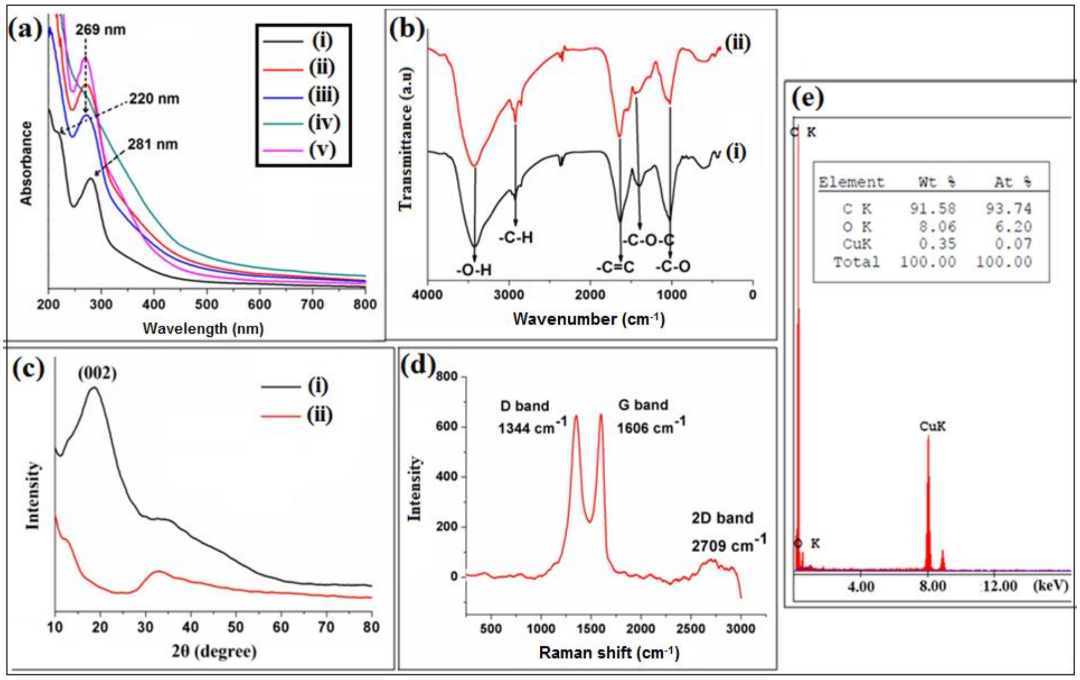

Element	Wt %	At %
C K	91.58	93.74
O K	8.06	6.20
CuK	0.35	0.07
Total	100.00	100.00

Figure 4A.1. (a) UV-visible spectra of (i) CD, (ii) *M. ferrea* Linn. reduced CD, (iii) tea reduced CD, (iv) *S. aromaticum* reduced CD and (v) *C. esculenta* reduced CD; **(b)** FTIR spectra of (i) RCD and (ii) sodium borohydride reduced CD (used for comparison purposes); **(c)** XRD patterns of (i) CD and (ii) RCD; **(d)** Raman spectrum of RCD; and EDX map of RCD.

To clarify the role of Fe^{3+} ions in reduction process of CD, an additional experiment was also conducted where we observed that CD was not reduced with only Fe^{3+} ions even after prolonged time. There was no red shift of the characteristic peak of CD in the UV visible spectrum of the solution containing CD and Fe^{3+} as shown in **Figure 4A.2**. This clearly indicates that Fe^{3+} is not a reductant in its bare state. However, as Fe^{3+} helps in complexation with the polyphenol compound and enhances the rate of reduction of CD, it is a promoter in this catalytic process. Further, literature supports the formation of H^+ ions and faster release of e^- during complexation of *C. esculenta* and Fe^{3+} ions, which have a strong influence in this reduction process [11]. From the above results it was observed that the preparation of RCD was the fastest and most effective using *C. esculenta* aqueous leaf extract in presence of Fe^{3+} ions, under normal atmospheric condition, so this process was used for further study.

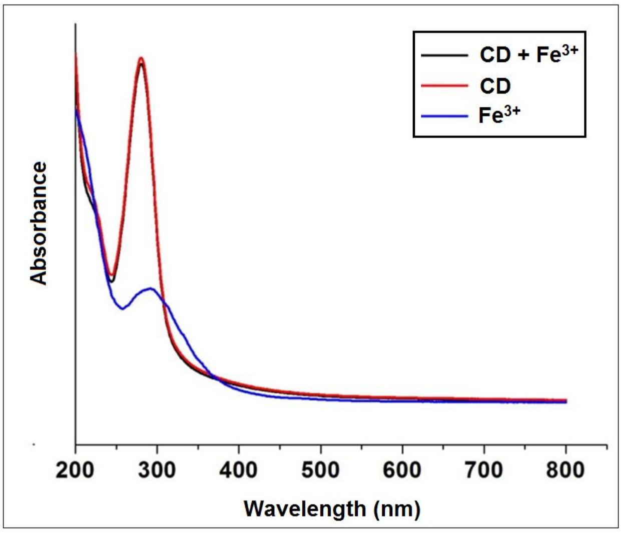

Figure 4A.2. UV visible spectra of Fe^{3+} ions, CD and a solution containing CD and Fe^{3+} ions.

The FTIR absorbance bands (ν max/cm^{-1}) like C=O (1731), C-O-C (1420), C-O (1266) and epoxy group (917) of CD (**Figure 4A.3a**) were diminished in RCD (**Figure 4A.1b**) [12]. The FTIR spectrum of RCD was also compared with CD reduced by sodium borohydride spectrum (**Figure 4A.1b** (ii)) to understand the reduction.

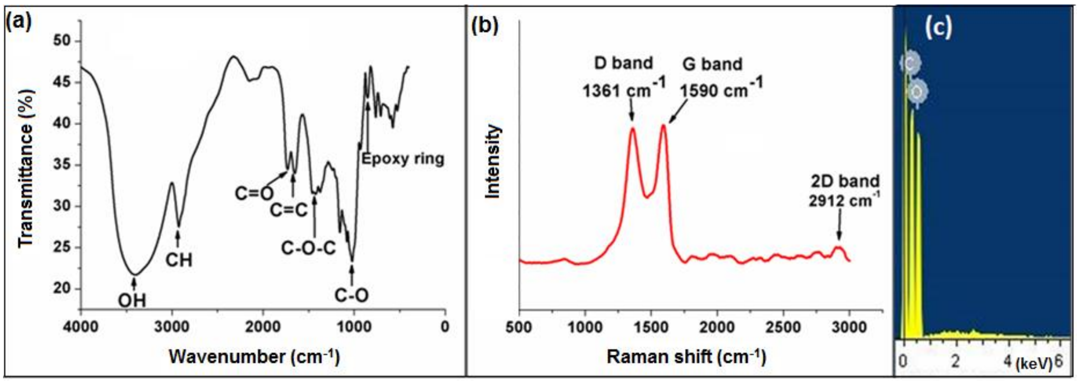

Figure 4A.3. (a) FTIR spectrum, **(b)** Raman spectrum; and **(c)** EDX map of CD.

The XRD patterns show that the broad peak of CD near 2θ ~ 21° was disappeared while peak near 32° was slightly sharpened in RCD (**Figure 4A.1c**), thus indicating the formation of a more graphitic structure [16]. The characteristic Raman D band (1361 cm^{-1}), G band (1590 cm^{-1}) and 2D band (2912 cm^{-1}) of RCD (**Figure 4A.1d**) clearly demonstrated the increase of I_D/I_G, as compared to CD (**Figure 4A.3b**), thus indicating multilayer graphitization of RCD. This is due to restoration of sp^2 carbon and decrease in the average sizes of the sp^2 domains upon reduction of CD, as well as due to the presence of unrepaired defects that remained even after the removal of oxygen moieties [17, 18]. This I_D/I_G ratio value is consistent with most chemical reduction reports of RGO [11, 19, 20]. In addition there is an increase in carbon to oxygen ratio (C/O) of RCD (11.2) in EDX analysis (**Figure 4A.1e**) as compared to CD (1.59) (**Figure 4A.3c**). HRTEM images confirmed the spherical shapes of RCD (**Figure 4A.4a**) with average size 3 nm and lattice spacing 0.20 nm.

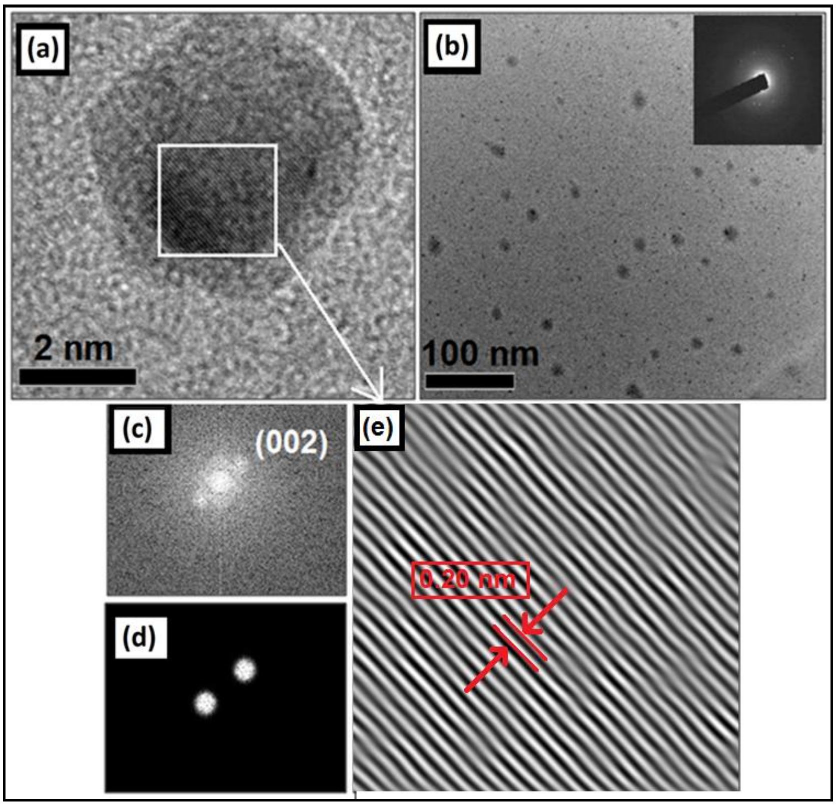

Figure 4A.4. **(a)** HRTEM image of RCD at 2 nm magnification; **(b)** particle distribution of RCD at 100 nm magnification with its SAED pattern as inset; FFT images of RCD phase **(c)** before masking, **(d)** after masking; and **(e)** IFFT of RCD phase showing the lattice fringes.

Poor crystalline nature of RCD was also supported by the selected area electron diffraction (SAED) pattern (inset of **Figure 4A.4b**). It is pertinent to mention that we also used the Bragg's equation to calculate the inter-planar distance (*d*) of RCD using the following equation.

$$d = n\lambda/2\sin\theta \ldots\ldots\ldots\ldots\ldots\ldots\ldots\ldots\ldots\ldots \textbf{(Eq. 4A.4)}$$

where n is the integer (1), λ is the wavelength of the of the incident X-ray beam (0.154 nm) at certain angle of incidence (theta, $\theta = 32°$).

Using the above equation, the lattice spacing of RCD was calculated to be 0.15 nm for the peak 32°, whereas from the TEM the lattice fringe was calculated to be 0.20. Thus the difference is not very significant. However, this little difference may be explained as follows. During TEM analysis, very dilute solution of the sample was taken and the lattice fringes were determined for a particular particle of RCD where the inter-planar spacing between the two planes was found to be 0.20 nm. On the other hand during XRD analysis the sample was taken in powdered state due to which agglomeration taken place which generates XRD peaks of many particles of different characters. Thus, the lattice fringe of RCD determined from TEM and XRD analyses may differ slightly.

4A.3.2. Optical properties

The UV-visible absorption spectrum for CD displayed absorption peaks around 220 nm, ascribed to π-π* transition of the conjugated C=C band and around 280 nm (through a tail extending into the visible range), credited to the n-π* transition of the C=O band as shown in **Figure 4A.1a** (i) [5]. However, upon reduction of CD, the band near 280 nm disappeared and a peak near 220 nm undergoes a red shift to 269 nm which indicates the restoration of conjugation and resulting in the formation of an aromatized multilayered structure (**Figure 4A.1a**) [11]. Further, RCD exhibited a broad absorption band over a wide range of wavelength from 250 to 800 nm, indicating effective photo-absorption which would be useful for its photocatalytic activity under visible light [21]. This broad absorption band over a wide range of wavelength is due to graphitic structure of RCD which has long π-π conjugation. The aqueous solutions of CD and RCD were found to be brown and dark brown in color, respectively, under daylight but exhibited blue and green fluorescence under UV light at different wavelengths as shown in **Scheme 4A.1**. Upon reduction of CD, the quantum yield increased from 9.6 to 18.5% (excited at 340 nm, using Quinine sulfate as reference). The characteristic features of the synthesized CD and

RCD are their emission wavelength and size dependent photoluminescence. From the PL spectra of CD and RCD at same concentration (10 mg mL^{-1}), it is clear that the intensity is dependent on their respective concentrations and excitation wavelengths (**Figure 4A.5**) [5, 22]. With an increase in the excitation wavelength, the emission peaks of both CD and RCD shifted to a higher wavelength, reaching fluorescence maximum while being excited at wavelength 340 nm, but subsequently decreasing upon further increasing the wavelength (**Figure 4A.5a** and **b**).

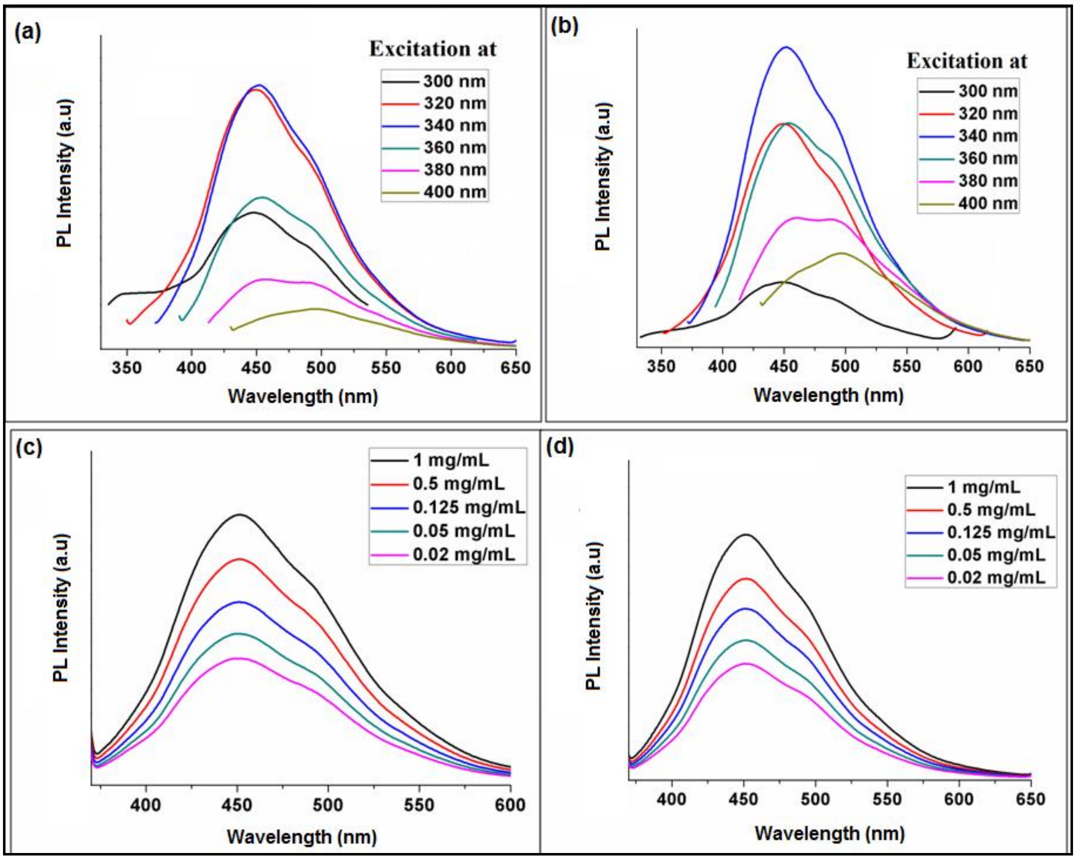

Figure 4A.5. PL spectra with variation of excitation wavelength 300-400 nm of (a) CD and (b) RCD; and PL spectra with variation of concentration of (c) CD and (d) RCD.

The highest PL intensity of CD and RCD was attributed to the maximum number of particles being excited at that wavelength and nature of their surfaces. The presence of polar functional groups on the surfaces of CD and RCD may result in a series of emissive traps between π and π^* of C=C. On illuminating CD and RCD at a certain excitation wavelength a surface energy trap dominates the emission [5]. The intensity of the PL spectra of CD and RCD also increased with the increase of their concentrations which may be attributed to the increasing interactions among the various surface polar groups at high concentration (**Figure 4A.5c** and **d**). The difference in the position of emission peak is due to the variation in size of the nanoparticles. Similar to semiconductor quantum dots, the energy gap of CD and RCD increases with the decrease in sizes and vice versa due to quantum effect. Thus the particles with a smaller size get excited at a lower wavelength, whereas larger size gets excited at higher wavelength [22, 23]. The enhanced green emission of the RCD is due to the zig-zag sites of its surfaces [1, 24]. The optical band gaps of CD and RCD were calculated from UV-visible spectra by using the following equation [8, 11].

$$\alpha = C(h\nu - E_{bulk})^{1/2}/h\nu \text{…………………………………..} \textbf{(Eq. 4A.5)}$$

Where α is absorption coefficient, C is a constant, h is the plank's constant, ν is the frequency and E_{bulk} is bulk 'band gap'. The band gaps were obtained by extrapolating the linear regression at $(\alpha h\nu)^2 = 0$ of the plot hν versus $(\alpha h\nu)^2$ (**Figure 4A.6a** and **b**).

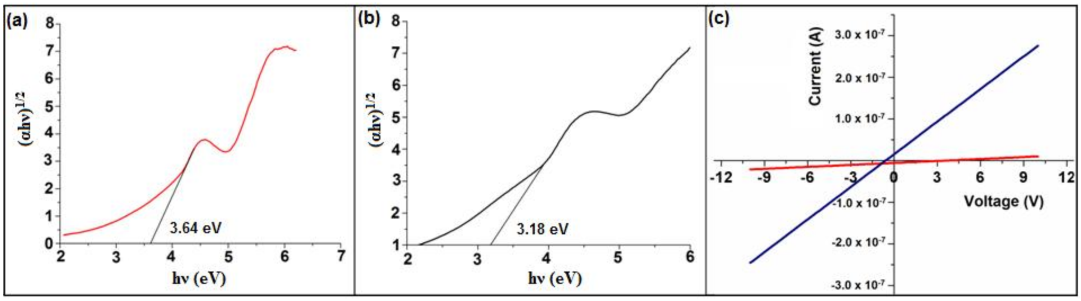

Figure 4A.6. $(\alpha h\nu)^{1/2}$ vs hν plots of **(a)** CD and **(b)** RCD; and **(c)** I-V curves for (i) RCD and (ii) CD.

The band gaps of CD and RCD were found to be 3.64 and 3.18 eV, respectively. The result indicates that the reduction of CD results in restoration of the π conjugated system. The obtained band gaps are in similar trend with the previously reported values of RGO and GO system [12, 25]. Further, contrary to the commercial TiO_2, CD and RCD belong to a class of carbonaceous organic semiconductors which provide a facile preparative route by using nontoxic chemicals, environmentally benign solvents and renewable precursors. Compared to traditional semiconductor catalysts like TiO_2, photoluminescent CD and RCD are superior in terms of functionalization, resistance to photo bleaching, toxicity and profound biocompatibility [3, 22]. In this regard, RCD may display an efficient visible light photocatalytic degradation of organic pollutants due to its strong visible light absorption band and enhanced fluorescence.

4A.3.3. Electrical conductivity

Electrical conductivities of CD and RCD were measured from their current-voltage (I-V) characteristics as obtained by a four probe setup (**Figure 4A.6c**). It was observed that RCD exhibited linear I-V relation with the voltage in the range of -10 to +10 V. However, I-V slope of CD was close to zero. This clearly indicates that, prior to reduction, CD behaved near to an insulating material which can be attributed to the presence of high oxygeneous groups. The structure of CD is predominantly amorphous owing to distortions from high fraction of sp^3-carbon. Moreover, the random distribution separates the sp^2-hybridized aromatized rings from the sp^3-hybridized rings which lead to the insulating nature of CD. However, the I-V slope of RCD significantly increased after its reduction demonstrating high electrical conductivity. Further, the linear behavior of the I-V curve of RCD indicated the formation of Ohmic contact between the graphitic structure and the electrodes. The enhanced electrical conductivity of RCD can be attributed to the removal of the oxygen functional groups and synchronized restoration of sp^2 carbon networks after reduction. The conductivities of CD and RCD were found to be 2.54×10^{-7} S m^{-1} and 2.53×10^{-6} S m^{-1}, respectively. The I-V measurement data, in conjunction with the Raman results, revealed that the conductivity of CD increased with increasing sp^2 carbon content and with increasing I_D/I_G value. The results follow a similar trend as reported by Lopez *et al.* where they showed that the chemical vapor deposition-graphene oxide (CVD-GO) exhibited an approximately linear rise of electrical conductively with increasing I_D/I_G [26].

It is pertinent to mention that this conductivity is not due to the presence of Fe^{3+} ions, as no traces of iron was present in RCD; confirmed from EDX analysis (no peak was observed for iron at ~ 6.4 keV) (**Figure 4A.1e**). Further, the qualitative test of aqueous ammonium thiocyanate (NH_4SCN) solution resulted in no color for aqueous dispersion of RCD, whereas it produces a blood-red color for the solution containing CD, phytoextract and Fe^{3+} ions.

4A.3.4. Thermal properties

CD exhibited a two-step thermal degradation pattern, whereas more steps were observed for RCD as shown in **Figure 4A.7**. In both the cases, initial (2-4)% weight loss near (110-112) °C may be assigned to loss of entrapped water molecules between the nanoparticles as they contain polar surface groups.

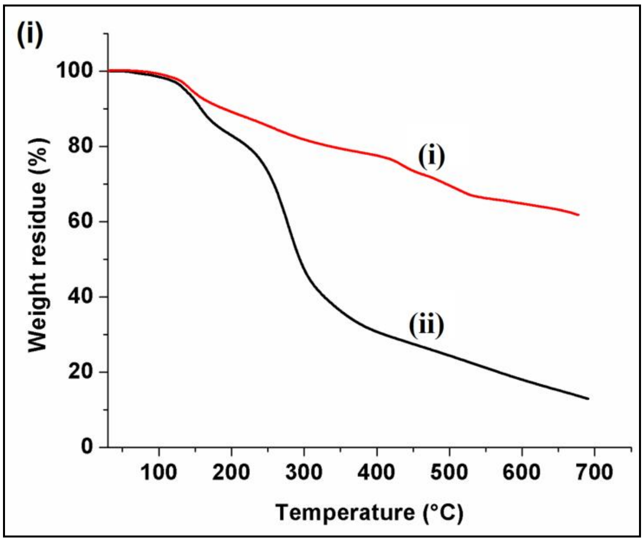

Figure 4A.7. TGA thermograms of (i) RCD and (ii) CD.

The actual initial degradation for CD and RCD commences near 200 °C which is due to the loss of labile oxygen containing functional groups (hydroxyl, epoxy, etc.). RCD exhibited a gradual loss of only 18 wt% up to 280 °C, which was much lower than CD where loss of 32 wt% up to 250 °C was observed. These results indicate a significantly decreased in amount of oxygenated functional groups in RCD. Further RCD showed less weight loss up to 250 °C and it exhibited a total weight loss of 38% between (500-800) °C. This may be attributed to the presence of phytoextract bound to the surface of RCD. This can be confirmed from the TGA curve of pure phytoextract which shows the same trend [27]. Therefore, RCD experiences (48-50)% less weight loss as compared to CD in the temperature range of (300-800) °C, which is also an indication of elimination of oxygeneous groups by reduction and higher thermal stability of RCD compared to CD. The residual weights obtained for CD and RCD at 800 °C was about 12% and 62%, respectively.

4A.3.5. Photocatalytic activity

The pathways for photocatalytic degradation of OC such as MB, MO, MB/MO mixture and BPA were studied by CD and RCD under normal solar light (not directly exposed under the sunlight) are shown in **Scheme 4A.3**. Actually, when RCD or CD nanoparticles were exposed to the OC solution, they absorbed visible light as well as near infrared light which led to the generation of e^-/hole (e^-/h^+) pairs in RCD/CD by excitation of valence band (VB) e^- [28].

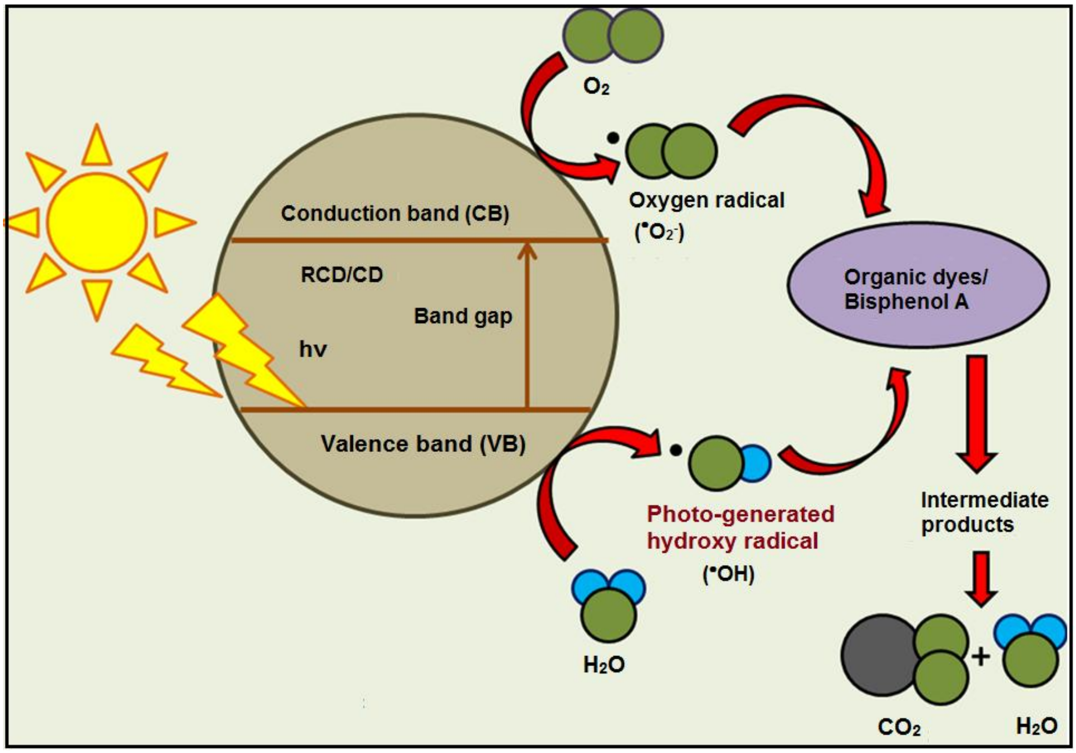

Scheme 4A.3. Proposed photocatalytic mechanism for degradation of organic pollutants by RCD and CD.

The formation of e^-/h^+ pairs in the RCD/CD photocatalyst is shown in **Eq. 4A.6** [29].

Photon activation: RCD/CD + hv $\longrightarrow e^- + h^+$ …………………… (**Eq. 4A.6**)

Consequently, the photo-generated e^- in RCD/CD easily react with the oxygen molecules (O_2) present in the aqueous medium to form superoxide radicals ($^\bullet O_2^-$) whereas the photo-generated holes in the VB react with water molecules to form hydroxyl radicals ($^\bullet OH$). These reactive oxidative species, $^\bullet O_2^-$ and $^\bullet OH$ degrade the organic molecules through an oxidative pathway, as described below in **Eq. 4A.7** and **Eq. 4A.8** [28].

Adsorbed oxygen: $(O_2)_{ads} + e^- \longrightarrow {}^\bullet O_2^-$ ……………………….. (**Eq. 4A.7**)

Water/moisture present, $H_2O + h^+ \longrightarrow {}^\bullet OH + H$ ……………….. (**Eq. 4A.8**)

Accordingly, the amounts of $^\bullet OH$ radical depend on the quantity of h^+ generated in RCD/CD. Furthermore, the quantity of h^+ also determines the ability of photocatalytic degradation. Subsequently, the organic pollutants are transformed into their degraded products by these active oxygen radicals into CO_2 and H_2O *via* photocatalytic pathways as shown in **Eq. 4A.9** and **Eq. 4A.10** [28, 29].

$R\text{-}H + {}^\bullet OH \longrightarrow {}^\bullet R + H_2O$ ……………………………... (**Eq. 4A.9**)

$^\bullet R + h^+ \longrightarrow {}^\bullet R^+ \longrightarrow CO_2 + H_2O$ …………….... (**Eq. 4A.10**)

It is pertinent to mention that RCD absorbs more visible light compared to CD, as revealed from their absorption spectra (degradation results are shown in **Figure 4A.8 - 4A.10**), which helps to increase the catalytic efficiency of RCD under solar light. RCD was finely ground by using a mortar and a pestle in order to increase its surface area.

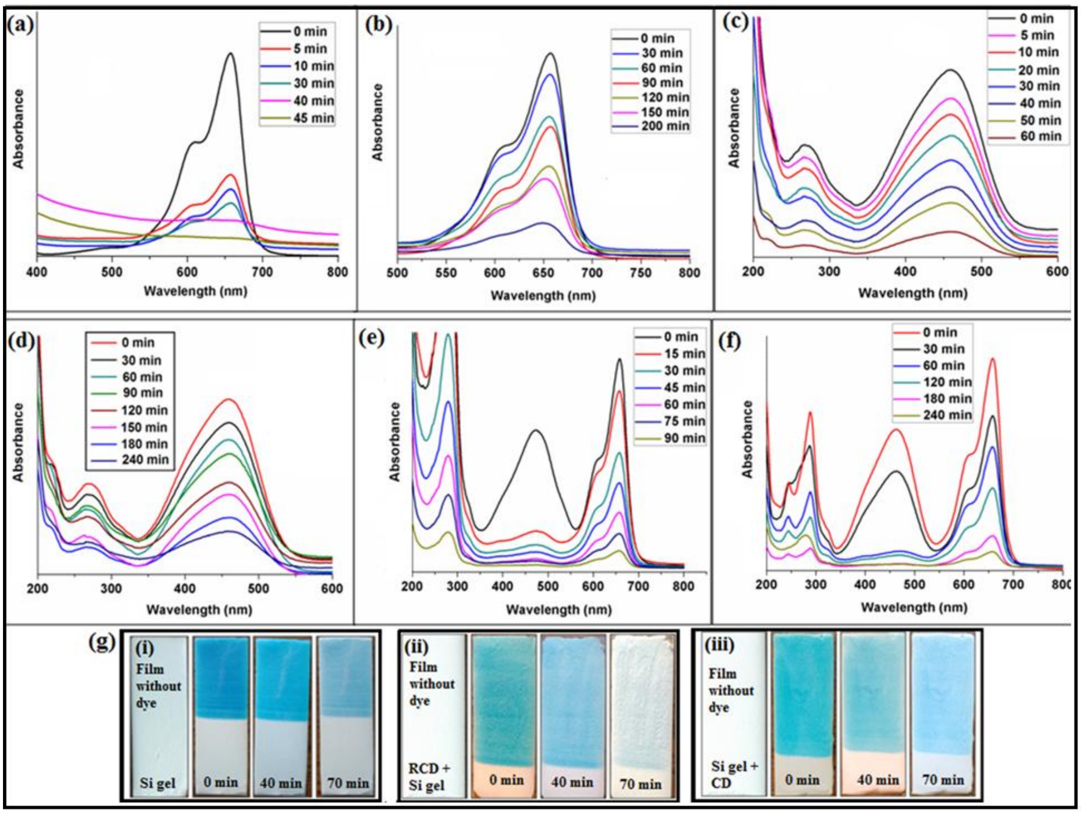

Figure 4A.8. Plots of UV absorbance against wavelength at different times for the degradation of MB in the presence of **(a)** RCD and **(b)** CD; plots of UV absorbance against wavelength for the degradation of MO in the presence of **(c)** RCD and **(d)** CD; and plots of UV absorbance against wavelength for the degradation of MB/MO mixture in the presence of **(e)** RCD and **(f)** CD; and **(g)** images showing the decolorization of MB by films of **(i)** silica gel, (ii) silica gel with RCD and (iii) silica gel with CD.

The concentration changes of the OC with time were monitored by UV absorbance. The plots of optical absorbance against wavelength for the degradation of the OC at different time intervals for both RCD and CD are shown in **Figure 4A.8** and **Figure 4A.9**. As we know, photocatalytic activity of a semiconductor is a result of the production of excited e^- under UV irradiation in its conduction band along with corresponding h^+ in the valence band, which react with contaminants adsorbed on the photocatalyst surface [6].

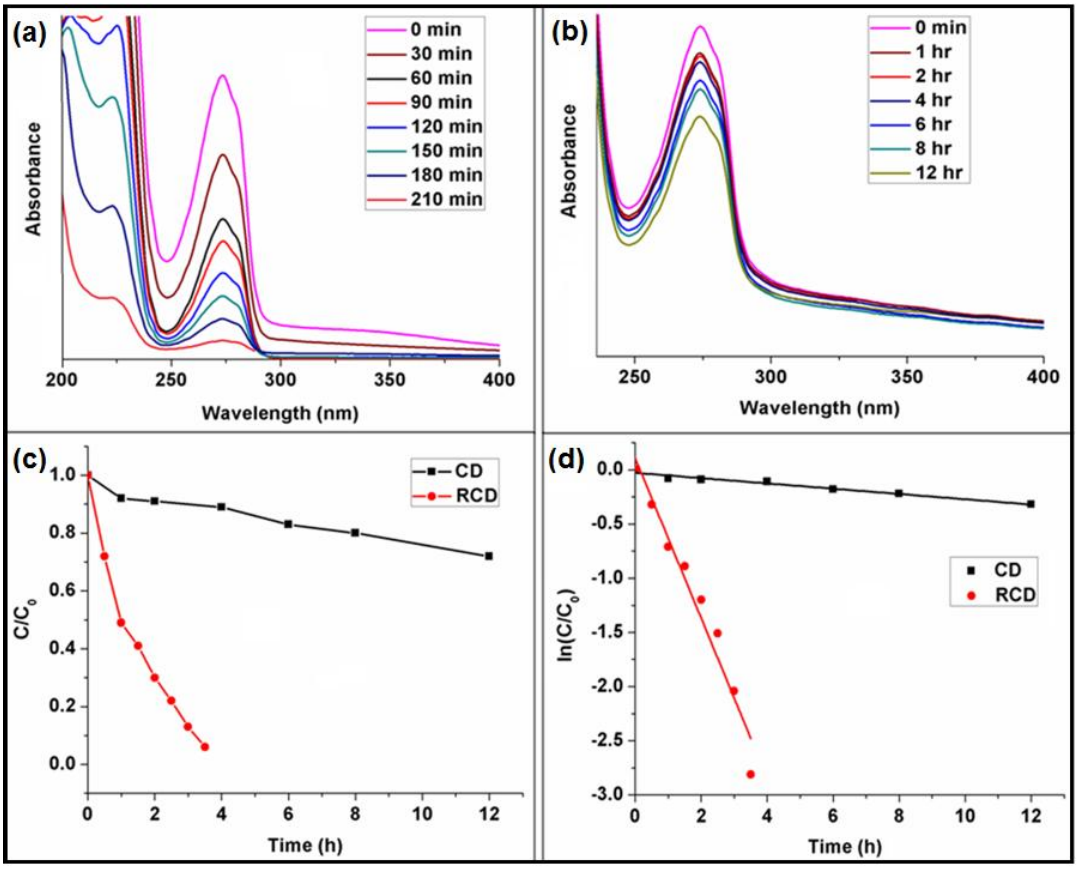

Figure 4A.9. Plots of UV absorbance against wavelength at different times for the degradation of BPA in the presence of **(a)** RCD and **(b)** CD; **(c)** degradation curves of aqueous solution of BPA; and **(d)** fitting degradation kinetic curves for BPA by CD and RCD.

The relatively larger band gap of CD reduces the efficiency of photocatalytic reactions due to low absorption capability of visible light and high recombination rate of photo-generated e^- and h^+ formed in the photocatalytic process. Due to the lower band gap of RCD (3.18 eV) than CD (3.64 eV), RCD has higher absorbance ability towards solar light than CD and thus the energy required for photo-generation of e^-/h^+ pair is relatively low [28]. Thus, the effective number of e^- generated for utilization in the degradation of OC is higher in RCD compared to those in CD. It is pertinent to mention that although recombination of e^- and h^+ in RCD takes place, the neat number of e^-/h^+ pairs required for generating $^\bullet O_2^-$ and $^\bullet OH$ to degrade the OC is higher than CD. Also RCD contains delocalized π e^- as it gets stability through the π conjugation in its aromatized structure which helps in reduction of e^-/h^+ recombination. Thus, RCD possesses a lower charge carrier recombination rate and higher surface adsorption capacity to hydroxyl groups than CD and hence its efficiency as a photocatalyst increased. Literature cites several reports on the photocatalytic degradation of BPA and organic dyes such as MB, MO and MB/MO mixture. The rates of degradation of MB, MO and MB/MO mixture with time for RCD and CD under solar light are shown in **Figure 4A.8** and **4A.10**. Tang *et al.* showed that using 0.3 g $CaIn_2O_4$ photocatalyst in 100 mL aqueous solution of MB at 47.8 µmol L^{-1} concentration, nearly 80% degradation was observed under visible light within 120 min [30]. Literature also reports that 0.1 g of TiO_2/ZnO photocatalyst can degrade 97% MO at 20 mg L^{-1} concentration 30 min of UV irradiation [31].

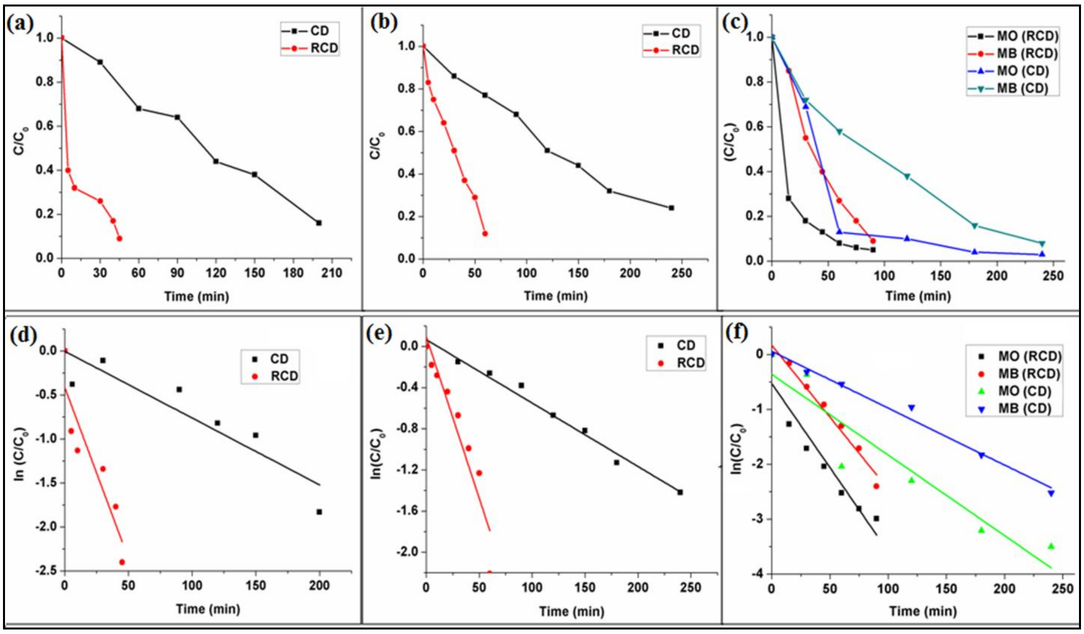

Figure 4A.10. Degradation curves of aqueous solutions of **(a)** MB, **(b)** MO and **(c)** MB/MO mixture; and fitting degradation kinetic curves for **(d)** MB, **(e)** MO and **(f)** MB/MO mixture using RCD and CD.

Conversely, 50 mg RCD can degrade 100% MB (10 ppm) and 96% MO (10 ppm) within just 45 min and 60 min of solar light irradiation, respectively (**Figure 4A.8a** and **c**). To examine the effect of loading and the superiority of RCD compared to CD, the dye degradation using CD was also tested as shown in **Figure 4A.8b** and **d**. CD took longer time for the same degradation of OC which was completed by RCD in a shorter time. The results clearly indicated the superiority of RCD as over CD. This is due to their ability to act as an efficient visible light assisted photocatalyst and not by the sensitization of dye molecules. Further, investigation of photocatalytic degradation activity of CD and RCD was conducted on the MB/MO mixture. After 15 min of solar irradiation, the intensity of UV absorption peak of MO was observed to decrease sharply in case of RCD, while intensity of UV absorption peak of MB still remains high level as shown in **Figure 4A.8e**. After subsequent visible light irradiation up to 90 min, a rapid degradation of MB was observed by RCD. However, both CD and RCD exhibited a complete higher degradation rate for MO in comparison to MB in the MB/MO mixture (**Figure 4A.8e** and **f**). The difference implies that RCD and CD exhibit a preferential photocatalytic degradation of MO in the MB/MO mixture. Lower degradation rate of MB in MB/MO mixture than individual MB solution is mainly associated to the occurrence of the competitive consumption of the oxidizing species in MO as well as that the presence of N=N which makes MO more reactive, whereas the presence of -CH_3 group in MB makes it resistant to photodegradation [27]. Literature sites similar preferences in the degradation between MB/MO mixture as reported previously for mesoporous $ZnO/ZnAl_2O_4$ powder [32] and NiO-Bi_2O_3 nanocomposite [33].

For the same reasons as stated above, RCD demonstrated superiority over CD when the self-cleaning property of RCD was examined by degradation of MB as model dirt on silica coated films under sunlight irradiation by visual means as shown in **Figure 4A.8g**. Both the nanomaterials, RCD and CD decolorize the solution of MB. For a better comparison, glass slides with silica and silica in the presence of RCD and CD films were dipped in aqueous solution of dye and exposed to sunlight. Upon exposure, time the change in color of the films is recorded at different times as shown in **Figure 4A.8g**. The photographs illustrate that RCD exhibits better decolorization of the model dirt over a period of 70 min in comparison to CD. Thus, it can be utilized as a material for designing of self-cleaning surfaces. Among various OC, BPA is known mostly difficult to be degraded under visible light and a number of reports have shown the photocatalytic degradation of BPA over semiconductor photocatalysts under UV light. Bechambi *et al.* reported that 1 g L^{-1} C-doped ZnO in 50 mg L^{-1} BPA in the presence of H_2O_2 at pH 8 effectively reached 100% BPA degradation and 70% BPA mineralization after 24 h of UV irradiation [8]. Wang *et al.* reported that 1% immobilized TiO_2 can degrade 97% BPA at 10 ppm concentration within 6 h upon UV radiation [34]. However, only a few reports on the photodegradation of BPA are found under visible light. Qu *et al.* showed that 10 mg CNT can photodegrade 74.8% BPA at 10 ppm concentration upon exposure of solar light for 180 min [9]. On the other hand, 50 mg of RCD can degrade 100% BPA at 50 mg L^{-1} concentration within 3.5 h under sunlight irradiation (**Figure 4A.9)**. The complete degradation of BPA by CD was only possible on exposure of UV light. Thus, the efficiencies of the reported catalysts in the degradation of MB, MO, MB/MO mixture and BPA is inferior as compared to the presently reported catalyst, where there is no need of any additional energy or materials, other than normal solar light. The present study demonstrated the degradation of MB, MO, MB/MO mixture and BPA using RCD under solar irradiation for the first time.

In all the above cases of photocatalytic degradation of OC, the photocatalytic activity of RCD is significantly faster than CD. This may be attributed to the presence of optimum level of polar functional groups that may interact with the OC and help to anchor on the surfaces. This helps in better interaction of OC with the active oxygen radicals. Thus, inspite of using an equal amount of nanoparticles in both the cases, the same extent of degradation was not observed under the same total period of exposure. The pseudo-first order kinetics model equation was used to describe the photo-degradation behavior of the nanomaterials as follows (**Figure 4A.9** and **4A.10**).

$-dC/dt = K_1t$………………………………………… (**Eq. 4A.11**)

where C = concentration of the OC at specific time t and K_1 = apparent rate constant. After integrating **Eq. 4A.11**, the following equation is obtained.

$\ln(C/C_0) = -K_1t$…………………………………... (**Eq. 4A.12**)

where C_0 is the initial concentration (at t = 0) of OC. The fitting plots of $\ln(C/C_0)$ versus time are shown in **Figures 4A.9d** and **4A.10d-f**, which demonstrate that the degradation of the OC is well described by pseudo-first order kinetics with the fitting coefficients over 0.8, indicating a regular photo-degradation behavior. Though CD nanoparticles degrade OC, their efficiencies are very poor due to their high recombination rate of photo generated e^-/h^+ pairs and low absorbance of visible light. Thus, CD is only useful under exposure of UV light, which hinders their practical applicability. Though literature also reported the degradation of MB and BPA using different nano photocatalysts, but in almost all the cases the photocatalytic degradation was studied under UV irradiation [7, 9]. The catalytic activity of these catalysts is inferior as compared to the presently reported RCD nanomaterial, where other than normal solar light no additional energy is needed. Again, to clarify the doubt of self-degradation of the dye a blank experiment was designed without using CD or RCD. No change in dye intensity (measured by UV-visible spectroscopy) even after 5 h of sunlight exposure in the absence of nanomaterial, clearly indicates that the dye degradation is not self-degradation (**Figure 4A.11a**).

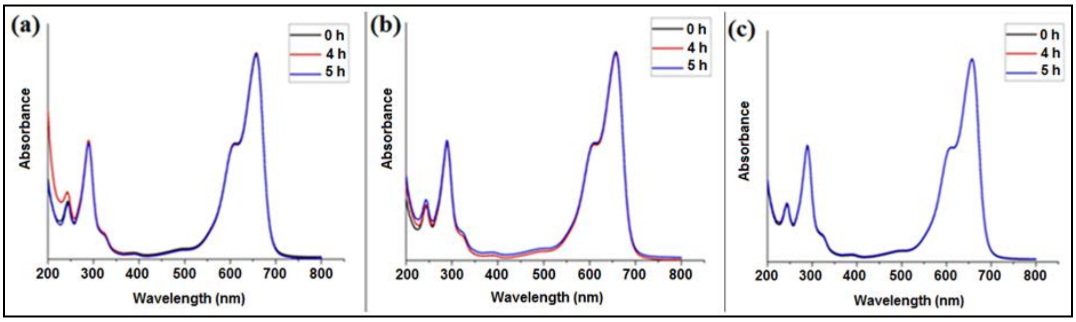

Figure 4A.11. Plots of UV absorbance against wavelength at different times for the degradation of MB **(a)** without nanomaterial under sunlight, with **(b)** RCD under darkness and **(c)** CD under darkness.

Further, no color change in the dye solution was observed even after exposure of 5 h sunlight (**Figure 4A.12**). In this context, another experiment of dye degradation with CD and RCD was performed under dark condition. In this case also no change in dye intensity was observed even after prolonged time, as measured by UV-visible spectroscopy (**Figure 4A.11b** and **c**).

All those above results are clearly indicating superior photocatalytic activity of RCD as compared to CD.

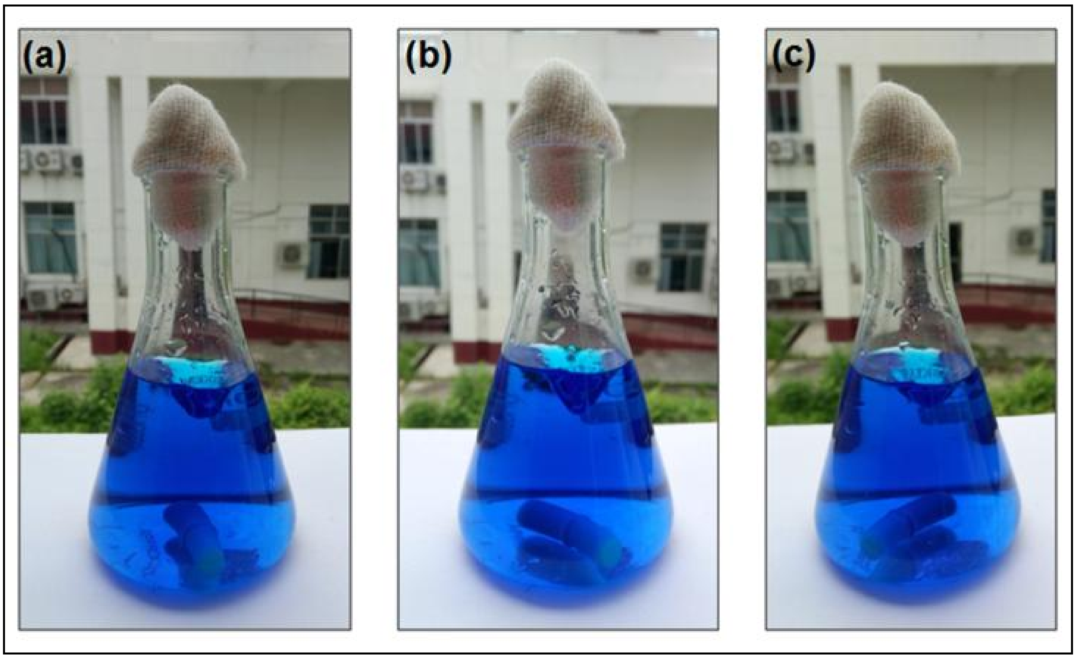

Figure 4A.12. MB dye solution without nanomaterial under sunlight at **(a)** 0 h, **(b)** after 4 h and **(c)** after 5 h under stirring.

4A.4. Conclusion

Thus, from this study, it can be concluded that bio-based carbon dot can be effectively reduced through a facile, green and eco-friendly one pot ultrafast route using aqueous phytoextract of C. *esculenta* in the presence of Fe^{3+} ions. It exhibited excellent excitation wavelength dependent fluorescence. This novel zero dimensional carbon based nanomaterial efficiently degraded organic pollutants like methylene blue, methyl orange, methylene blue/methyl orange mixture and bisphenol A under normal solar radiation. Reduced carbon dot demonstrated higher and more efficient photocatalytic degradation as compared to carbon dot, following the pseudo-first-order kinetics model. In a nutshell, environmentally friendly reduced carbon dot may open up a new avenue for its practical applications as a photocatalyst for efficient and economical elimination of pollutants towards secure and sustainable environment.

References

[1] Zheng, H., Wang, Q., Long, Y., Zhang, H., Huang, X., and Zhu, R. Enhancing the luminescence of carbon dots with a reduction pathway. *Chemical Communication*, 47(38):10650-10652, 2011.

[2] Zhuo, Y., Zhong, D., Miao, H., and Yang, X. Reduced carbon dots employed for synthesizing metal nanoclusters and nanoparticles. *RSC Advances*, 5(41):32669-32674, 2015.

[3] Lim, S. Y., Shen, W., and Gao, Z. Carbon quantum dots and their applications. *Chemical Society Reviews,* 44(1):362-381, 2015.

[4] Thakur, S. and Karak, N. Alternative methods and nature-based reagents for the reduction of graphene oxide: a review. *Carbon*, 94:224-242, 2015.

[5] De, B. and Karak, N. A green and facile approach for the synthesis of water soluble fluorescent carbon dots from banana juice. *RSC Advances*, 3(22):8286-8290, 2013.

[6] Hazarika, D. and Karak, N. Photocatalytic degradation of organic contaminants under solar light using carbon dot/titanium dioxide nanohybrid, obtained through a facile approach. *Applied Surface Science,* 376:276-285, 2016.

[7] Chiang, K., Lim, T. M., Tsen, L., and Lee, C. C. Photocatalytic degradation and mineralization of bisphenol A by TiO_2 and platinized TiO_2. *Applied Catalysis A: General,* 261(2):225-237, 2004.

[8] Bechambi, O., Sayadi, S., and Najjar, W. Photocatalytic degradation of bisphenol A in the presence of C-doped ZnO: effect of operational parameters and photodegradation mechanism. *Journal of Industrial and Engineering Chemistry*, 32:201-210, 2015.

[9] Qu, J., Cong, Q., Luo, C., and Yuan, X. Adsorption and photocatalytic degradation of bisphenol A by low-cost carbon nanotubes synthesized using fallen leaves of poplar. *RSC Advances*, 3(3):961-965, 2013.

[10] Fan, F., Wang, X., Ma, Y., Fu, K., and Yang, Y. Enhanced photocatalytic degradation of dye wastewater using ZnO/reduced graphene oxide hybrids. *Fullerenes, Nanotubes, and Carbon Nanostructures*, 23(11):917-921, 2015.

[11] Thakur, S. and Karak, N. Multi-stimuli responsive smart elastomeric hyperbranched polyurethane/reduced graphene oxide nanocomposites. *Journal of Material Chemistry A*, 2(36):14867-14875, 2014.

[12] Thakur, S. and Karak, N. Green reduction of graphene oxide by aqueous phytoextracts. *Carbon*, 50(14):5331-5339, 2012.

[13] Chakraborty, P., Deb, P., Chakraborty, S., Chatterjee, B., and Abraham, J. Cytotoxicity and antimicrobial activity of Colocasia esculenta. *Journal of Chemical and Pharmaceutical Research*, 7(12):627-635, 2015.

[14] Markova, Z., Novak, P., Kaslik, J., Plachtova, P., Brazdova, M., Jancula, D., Siskova, K. M., Machala, L., Marsalek, B., Zboril, R., and Varma, R. Iron(II,III)-polyphenol complex nanoparticles derived from green tea with remarkable ecotoxicological impact. *ACS Sustainable Chemistry & Engineering*, 2(7):1674-1680, 2014.

[15] Dey, R. S., Hajra, S., Sahu, R. K., Raj, C. R., and Panigrahi, M. K. A rapid room temperature chemical route for the synthesis of graphene: metal-mediated reduction of graphene oxide. *Chemical Communications*, 48(12):1787-1789, 2012.

[16] Stobinski, L., Lesiak, B., Malolepszy, A., Mazurkiewicz, M., Mierzwa, B., Zemek, J., Jiricek, P., and Bieloshapka, I. Graphene oxide and reduced graphene oxide studied by the XRD, TEM and electron spectroscopy methods. *Journal of Electron Spectroscopy and Related Phenomena,* 195:145-154, 2014.

[17] Cui, P., Lee, J., Hwang, E., and Lee, H. One-pot reduction of graphene oxide at subzero temperature. *Chemical Communications,* 47(45):12370-12372, 2011.

[18] Stankovich, S., Dikin, D. A., Piner, R. D., Kohlhaas, K. A., Kleinhammes, A., Jia, Y., Wu, Y., Nguyen, S. T., and Ruoff, R. S. Synthesis of graphene-based nanosheets via chemical reduction of exfoliated graphite oxide. *Carbon*, 45(7):1558-1565, 2007.

[19] Zhou, Y., Bao, Q., Tang, L. A. L., Zhong, Y., and Loh, K. P. Hydrothermal dehydration for the "green" reduction of exfoliated graphene oxide to graphene and demonstration of tunable optical properties. *Chemistry of Materials*, 21(13):2950-2956, 2009.

[20] Dong, Y., Niu, X., Song, W., Wang, D., Chen, L., Yuan, F., and Zhu, Y. Facile synthesis of vanadium oxide/reduced graphene oxide composite catalysts for enhanced hydroxylation of benzene to phenol. *Catalysts,* 6(5):74, 2016.

[21] Zhu, S., Song, Y., Zhao, X., Shao, J., Zhang, J., and Yang, B. The photoluminescence mechanism in carbon dots (graphene quantum dots, carbon nanodots, and polymer dots): current state and future perspective. *Nano Research*, 8(2):355-381, 2015.

[22] Gogoi, S., Kumar, M., Mandal, B. B., and Karak, N. High performance luminescent thermosetting waterborne hyperbranched polyurethane/carbon quantum dot nanocomposite with in vitro cytocompatibility. *Composites Science and Technology*, 118:39-46, 2015.

[23] Sahu, S., Behera, B., Maiti, T. K., and Mohapatra, S. Simple one-step synthesis of highly luminescent carbon dots from orange juice: application as excellent bio-imaging agents. *Chemical Communications*, 48(70):8835-8837, 2012.

[24] Xu, Y., Wu, M., Feng, X. Z., Yin, X. B., He, X. W., and Zhang, Y. K. Reduced carbon dots versus oxidized carbon dots: photo- and electrochemiluminescence investigations. *Chemistry-A European Journal,* 19(20):6282-6288, 2013.

[25] Loh, K. P., Bao, Q., Eda, G., and Chhowalla, M. Graphene oxide as a chemically tunable platform for optical applications. *Nature Chemistry*, 2(12):1015-1024, 2010.

[26] Lopez, V., Sundaram, R. S., Gómez-Navarro, C., Olea, D., Burghard, M., Gomez-Herrero, J., Zamora, F., and Kern, K. Chemical vapor deposition repair of graphene oxide: a route to highly-conductive graphene monolayers. *Advanced Materials,* 21(46):4683-4686, 2009.

[27] Khan, M., Al-Marri, A. H., Khan, M., Mohri, N., Adil, S. F., Al- Warthan, A., Siddiqui, M. R. H., Alkhathlan, H. Z., Berger, R., Tremel, W., and Tahir, M. N.

Pulicaria glutinosa plant extract: a green and ecofriendly reducing agent for the preparation of highly reduced graphene oxide. *RSC Advances*, 4(46):24119-24125, 2014.

[28] Wong, C. P. P., Lai, C. W., Lee, K. M., and Hamid, S. B. A. Advanced chemical reduction of reduced graphene oxide and its photocatalytic activity in degrading reactive black 5. *Materials*, 8(10):7118-7128, 2015.

[29] Colmenares, J. C. and Luque, R. Heterogeneous photocatalytic nanomaterials: prospects and challenges in selective transformations of biomass-derived compounds. *Chemical Society Reviews,* 43(3):765-778, 2014.

[30] Tang, J., Zou, Z., Yin, J., and Ye, J. Photocatalytic degradation of methylene blue on $CaIn_2O_4$ under visible light irradiation. *Chemical Physics Letters*, 382(1-2):175-179, 2003.

[31] Zha, R., Nadimicherla, R., and Guo, X. Ultraviolet photocatalytic degradation of methyl orange by nanostructured TiO_2/ZnO heterojunctions. *Journal of Materials Chemistry A*, 3(12):6565-6574, 2015.

[32] Huo, R., Kuang, Y., Zhao, Z., Zhang, F., and Xu, S. Enhanced photocatalytic performances of hierarchical ZnO/$ZnAl_2O_4$ microsphere derived from layered double hydroxide precursor spray-dried microsphere. *Journal of Colloid and Interface Science,* 407:17-21, 2013.

[33] Hameed, A., Gombac, V., Montini, T., Graziani, M., and Fornasiero, P. Synthesis, characterization and photocatalytic activity of NiO-Bi_2O_3 nanocomposites. *Chemical Physics Letters,* 472(4-6):212-216, 2009.

[34] Wang, R., Ren, D., Xia, S., Zhang, Y., and Zhao, J. Photocatalytic degradation of Bisphenol A (BPA) using immobilized TiO_2 and UV illumination in a horizontal circulating bed photocatalytic reactor (HCBPR). *Journal of Hazardous Materials*, 169(1-3):926-932, 2009.

4B. Fabrication of starch modified hyperbranched polyurethane nanocomposite with reduced carbon dot

4B.1. Introduction

As stated in **Chapter 3** and in introduction of **Sub-Chapter 4A**, the development of a bio-based SMP with sufficient mechanical strength is still a crucial challenge in the field of biomedical. In this context, starch modified HPU nanocomposite using RCD is developed to enhance the mechanical attributes as well as the thermoresponsive shape memory behavior of HPU for advanced biomedical applications. Such improvements in properties prove to be crucial in achieving remarkable self-tightening behavior at body temperature such as wound closure in orthopedic surgery [1]. Accurate wound closure is primarily aimed at rapid skin healing with minimum risk of complications such as wound infection or dehiscence which causes morbidity and delayed discharge of the patient [2]. In this context, sutures (natural/synthetic) are one of the most commonly used methods of wound closure post endoscopic surgery with a huge global market [2, 3]. They are implantable medical devices which ligate blood vessels and hold body tissues together to assist and accelerate the healing process with negligible or no scar formation in a surgical procedure or an injury [4]. The advantage of absorbable sutures (polydioxanone, poly(glycolic acid), catgut etc.) over non-absorbable (nylon, stainless steel, polyester, etc.) is that the formers are absorbed over time in the host body [5]. Non-absorbable sutures are often left in the body permanently under *in vivo* conditions and hence require removal to prevent side effects of the body such as excessive scarring, formation of stitch abscess and stitch sinus [6]. On the contrary, synthetic absorbable sutures do not require a second surgery, as no foreign substance is left permanently in patient body which could create any long term problem [5, 6]. It is pertinent to mention that sutures require securing of wounds by knots with sufficient strength and a negligible residual compression and tension on the tissues during wound closure. However, even with absorbable sutures, medical practitioners are not able to make a proper knot during the process of suturing to ensure optimal tissue closure strength. A tight knot may lead to damage of healthy cells by causing skin necrosis and infection [7]. Also, an improperly sealed wound line will not be sufficient to avoid infiltration of foreign bodies [8].

Hence, there is a genuine need of a suture material that can smartly tighten as per requirement with devoid of any human intervention. Thus, smart suturing with efficient shape recovery under body temperature is considered to be most significant. In this context, the use of biodegradable SMP as sutures not only actuates the shape change after insertion into the human body but also avoids a second surgery for its removal. Lendlein and Langer showed the first demonstration of SMP in medical applications with the self-tightening biodegradable suture for minimum invasive surgery [9]. However, absorbable polymeric sutures suffer from inadequate mechanical strength and structural characteristics to match the basic bio-chemico-mechanical requirements for their proper functioning [10]. Bichon *et al.* reported that catgut suture suffer from drawbacks such as quick loss of tensile strength and strong inflammation reaction within the first three days of implantation [11]. After induction of the degradation process, the polymeric sutures gradually lose their mechanical properties.

In this regard, the previous chapter discussed the potentiality of RCD to confer a strong physicochemical interaction with the similar polar functional group containing HPU matrix owing to its optimum functionality of polar peripheral groups. The optimum functionality of the graphitic RCD serves for strong interaction with the large polar surface functional groups of HPU as well as host cells, confined geometry with desired void spaces, high solubility with good compatibility etc [12, 13]. In this context, starch modified HPU might be the right option as the matrix because of its improved biodegradability, biocompatibility, flexibility and fascinating cell adherence aptitude, as mentioned in **Chapter 2**. Thus, the judicious incorporation of RCD into the biodegradable, biocompatible starch modified HPU matrix with fascinating cell adherence aptitude is suitable for obtaining the targeted suturing system. Moreover, no literature on starch based HPU/RCD nanocomposites has been reported till date as a self-tightening suture for biomedical applications.

Therefore, in the present study, starch modified HPU/RCD nanocomposite was *in situ* fabricated as a high performing sustainable, tough suture. The thermo responsive shape memory behavior, physico-mechanical, thermal and biological properties were investigated for their utilization as suturing material in biomedical applications.

4B.2. Experimental

4B.2.1. Materials

Polycaprolactone diol (PCL), toluene diisocyanate (TDI), 1,4-butanediol (BD), starch, ethanol, xylene and N, N-dimethylacetamide of similar specifications and grade were used as described in **Chapter 2** (**Section 2.2.1**) and **Chapter 3** (**Section 3.2.1**). Hyperbranched starch modified polyol (HBSP) was prepared using the same method as described in **Chapter 2** (**Section 2.2.3.1**). RCD was synthesized using the same technique as described in **Sub-Chapter 4A** (**Section 4A.2.2.2**).

Further, phosphate buffered saline (PBS, pH 7.4, Hi-Media, India), Heparin (Sigma Aldrich, USA), TritonX-100 (Sigma Aldrich, USA) lactate dehydrogenase (LDH) kit (Sigma Aldrich, USA), *Clostridium histolyticum* (Sigma Aldrich, USA), Dulbecco's Modified Eagle’s Medium (DMEM; Gibco, USA), fetal bovine serum (FBS, Gibco, USA), Alamar Blue (Invitrogen, USA) and neutral buffered saline (NBF, Sigma Aldrich, USA) used in the biological evaluation of the nanocomposite films were of same grade and specifications as mentioned in **Chapter 3** (**Section 3.2.1**). Enzyme-Linked Immunosorbent Assay (ELISA) kit (Invitrogen, USA) and lipopolysaccharide (LPS from *E. coli*, Sigma Aldrich, USA) were used to study the *In vitro immunocompatibility* of the nanocomposites. Endothelial cell growth supplement (ECGS, Sigma Aldrich, USA), antibiotic-antimycotic solution (Himedia, India) and smooth muscle growth supplement (SMGS, Invitrogen, USA) were used in the Isolation and culture of vascular cells. Calcein AM fluorescent dye (Sigma Aldrich, USA) and Hoechst 33342 (Sigma Aldrich, USA) were used in the *in vitro* cytocompatibility assessment of the nanocomposite films.

4B.2.2. Methods

4B.2.2.1. Fabrication of HPU nanocomposites

HPU/RCD nanocomposite was fabricated by an *in situ* approach [14]. Briefly, TDI (0.007 mol, 1.22 g), PCL (6 g, 0.002 mol) and 0.36 g BD (0.36 g, 0.004 mol) were reacted in a round bottom flask, fitted with a mechanical stirrer at (70 ± 2) °C for 3 h under nitrogen gas flow (-NCO/-OH = 1). In the second step, HBSP and remaining amount of TDI were added into the reaction mixture using xylene as the solvent at room temperature (-NCO/-OH = 1). Gradually, the temperature was raised to (80 ± 2) °C and continuously stirred for 2 h. A dispersion of RCD in DMAc was incorporated at room temperature and the reaction mixture was made to run at (80 ± 2) °C for 2 h for completion. Three different compositions of in situ bio-based nanocomposites were prepared using 0.5, 1.0 and 2.0 wt% of RCD, which are encoded as HPU/RCD0.5, HPU/RCD1 and HPU/RCD2, respectively. Likewise, HPU was also prepared by following the same method without the incorporation of any nanomaterial for comparison purposes.

4B.2.2.2. In vitro degradation study

The *in vitro* degradation of the nanocomposite films was conducted in accordance with ASTM standard method [15, 16]. The films were incubated in 0.1 M PBS at 37 °C in a shaking incubator set at 30 rpm over a period of 90 days. The thickness of the films was 0.5 ± 0.01 mm. The experiment was carried out in triplicates and the film to PBS weight ratio was maintained at 1:3 ratio. At regular interval of 30, 60, and 90 days of test, films were taken out of PBS, washed with deionized water and dried at 37 °C. The percentage mass loss was calculated from the equation below.

$$\text{Degradation (\%)} = [(W_0 - W_1)/W_0] \times 100 \ \ldots\ldots\ldots\ldots\ldots \ (\textbf{Eq. 4B.1})$$

Where, W_0 = initial dry weight of the film and W_1 = final dry weight of the film.

4B.2.2.3. Lactate dehydrogenase activity

The *in vitro* quantification of the activated platelets adhered on to the HPU/RCD nanocomposite films were measured by assessing the LDH activity [17]. Whole blood was collected from porcine source and primed with heparin (5 U mL^{-1}). Blood was centrifuged at 150 g for 10 min at 22 °C, yielding yellowish top layer of platelet rich plasma (PRP). The films having uniform surface area were incubated with platelet rich plasma (PRP) at 37 °C for 1 h and the adhered platelets were lysed with 1% TritonX-100 for 1 h at 37 °C. Platelet lysate was collected and centrifuged at 10,000 rpm at 4 °C. LDH activity was measured using LDH kit according to manufacturer’s instructions and reported as milliunits mL^{-1}. Amount of LDH corresponds to the number of adhered platelets on the films.

4B.2.2.4. Hemolytic activity

Hemolytic activity was assessed by quantifying the amount of lysis of red blood cell(s) (RBC) induced by HPU/RCD nanocomposite films as per previously mentioned in **Chapter 3** (**Section 3.2.3.9**). Porcine whole blood was collected in heparin containing vial and centrifuged at 500 g at room temperature for 5 min. The yellowish upper layer containing the plasma was discarded. The bottom layer containing the RBC was washed twice with 150 mM NaCl buffer and diluted for 20 times. An amount of 200 μL of diluted blood was incubated with the films for 1 h at room temperature. For positive and negative controls, 20% TritonX-100 in PBS and 150 mM NaCl buffer were used, respectively. The film treated blood was pelleted down at 3000 rpm to obtain undamaged RBC. Hemotytic activity was quantified by reading the absorbance of the supernatant at 540 nm in a multiplate reader.

4B.2.2.5. In vitro immunocompatibility assessment

Mouse macrophages (RAW 264.7) were stimulated with the nanocomposite films and the released tumor necrosis factor alpha (TNF-α) was measured as per previous reports [18, 19]. RAW 264.7 cells were seeded at 1 × 10^5 cells per well in 12-well tissue culture plate and incubated overnight. Films were added to cell confluent wells and incubated for 12 h. The medium was collected and assayed for TNF-α release by ELISA as per manufacturer's instructions. Briefly, the diluted medium was taken and incubated with biotinylated secondary antibody. Post incubation, the wells were washed, strepavidin-HRP working solution was added and further incubated at room temperature. Further, stabilized chromogen solution and stop solution were added and absorbance was recorded at 450 nm. Amount of TNF-α secreted was calculated using standard curve plot in the range of 0-1000 pg m L^{-1} murine TNF-α. Medium without film incubation was used as a negative control, while LPS (500 mg mL^{-1}) was used as positive control.

4B.2.2.6. Isolation and culture of vascular cells

For isolation of primary vascular cells, a portion of descending porcine aorta was procured from local slaughter house and smooth muscle cell(s) (SMC) and endothelial cell(s) (EC) were isolated as per modified earlier reports [18, 20]. Briefly, the outermost adventitial fibroblast layer was peeled off and remaining part was digested with 0.01% collagenase IA from *Clostridium histolyticum*. Post 1 h treatment, EC was scraped off from the luminal surface using a sterile scarper and maintained in DMEM complemented with 10% FBS, 200 μg mL^{-1} ECGS and 1% antibiotic-antimycotic solution. Residual part containing SMCs was further digested with identical enzyme solution for 8 h and obtained cell suspension was cultured in DMEM with 10% FBS, 50 μL mL^{-1} SMGS and 1% antibiotic-antimycotic solution. Cells were maintained in a humidified CO_2 incubator at 37 °C and 5% CO_2 and media was changed every alternative day. Cells of passage 3-6 were used for experiments.

4B.2.2.7. In vitro cytocompatibility

Cytocompatibility of the HPU/RCD nanocomposite films was evaluated by live cell imaging and Alamar blue assay for cellular viability and proliferation, respectively [18, 21, 22]. SMC and EC were used for the cytocompatibility assays. The films (ϕ 6 mm x 1 mm thickness) were sterilized using 70% v/v aqueous ethanol, washed with PBS (pH 7.4) and preconditioned with DMEM prior to cell seeding. Seeding density ($\sim 5 \times 10^4$ cells per film) and experiment time points for both cell types were kept identical to facilitate comparison. Live cell imaging was performed using 4 mM calcein AM fluorescent dye. The cell-seeded films were rinsed with PBS and incubated with live cell staining calcein AM dye solution for 20 min at 37 °C. Films were washed and imaged under fluorescent microscope. Further, to visualize cellular arrangement and cell adhesion, cells were fixed using NBF and nuclei were stained with Hoechst 33342 for 30 min under dark conditions followed by imaging. Cells seeded on tissue culture plate (TCP) were used as control. Equal number of cells ($\sim 5 \times 10^4$) was seeded on each film and the proliferation was assessed using Alamar Blue assay on day 1, 4 and 7 following manufacture’s protocol. In brief, the cell-seeded films were incubated in a medium containing 10% (v/v) Alamar Blue dye for 3 h at 37 °C in a 5% CO_2 incubator. Post incubation, 100 µL media containing dye was withdrawn and absorbance was recorded at 570/600 nm with a multiplate reader. All assays were performed in triplicate.

4B.2.2.8. Statistical analysis

All experiments were performed at least in triplicates (n = 3). Data are represented as mean ± standard deviation. One way ANOVA was performed using Microcal OriginPro 8 software to determine statistical significance ($^{\#}p \leq 0.05$ was considered as significant and $^{\#\#}p \leq 0.01$ as highly significant).

4B.2.2.9. Smart suture self-tightening study

In order to study the self-tightening behavior of HPU nanocomposites, the strip sample (100 mm x 1 mm x 0.4 mm in dimension) was heated at 70 °C for 5 min and stretched with a strong controlled force, to twice their original length (l_0). The stretched length was denoted as l_1. Immediately, the stretched samples were immersed at -(15 ± 5) °C in an ice-water salt bath for 10 min to fix the temporary shape. The shape fixity of the cooled nanocomposite films was noted by vacuum drying and placing for 30 min at room temperature (25 °C). The consequential length was subsequently measured and designated as l_2. Consequently, the fixed film was made into a loose knot in its temporary shape. The film was then exposed to a temperature of (37 ± 1) °C, during which the required time for self-tightening was noted. For the measurement of shape recovery, the sample without knot was used and the recovered length was denoted as l_3. The shape fixity (%) and shape recovery (%) was calculated from the equations as shown below:

Shape fixity (%) = $[(l_2 - l_0)/l_0] \times 100$ …………………..….. (**Eq. 4B.2**)

Shape recovery (%) = $[(l_1 - l_3)/l_0] \times 100$.......................... (**Eq. 4B.3**)

The test was repeated 5 times and the results were consistent.

4B.2.3. Characterization

Fourier Transformed Infrared (FTIR) and X-ray diffraction (XRD) analyses of HPU/RCD nanocomposites were conducted under same conditions and by using the same instrument as mentioned **in Chapter 2** (**Section 2.2.2**). The size, shape and distribution of the RCD within the HPU matrix were studied from High Resolution Transmission Electron Microscopic (HRTEM) by employing the same instrument as mentioned in **Chapter 3** (**Section 3.2.2**). Thermogravimetric analysis (TGA), differential scanning calorimetric (DSC), Universal Testing Machine (UTM) and impact tester were employed to study the HPU/RCD nanocomposites using the same instruments as mentioned in **Chapter 2** (**Section 2.2.2**). Hardness of the HPU/RCD nanocomposite films were evaluated by using a hardness tester (Shore A Hardness Tester, MGW Precision, Maharashtra, India). The surface morphology of the nanocomposites was studied by a Field Emission Scanning Electron Microscope (FESEM, Zeiss, Sigma), after platinum coating on the surface. Fluorescently labelled platelets were imaged under a fluorescent microscope (EVOS FL, Life Technologies, USA). Multiplate reader (Tecan, Infinite M200, Switzerland) was used for the determination of the absorbance values in the hemolytic and Alamar Blue assays.

4B.3. Results and discussion

4B.3.1. Fabrication of HPU nanocomposites

The RCD nanocomposite was fabricated by means of *in situ* polymerization technique using HBSP as branching moiety and 0.5, 1.0 and 2 wt% of RCD into the HPU matrix, separately (**Scheme 4B.1**). At the start of second step of the reaction, HBSP was added very slowly as a dilute solution (15% in xylene) in order to avoid gel formation. Although the greater extent of the reaction is completed at this stage of the reaction, the FTIR analysis of the reaction mixture shows a band at 2270 cm^{-1} indicating the presence of free –NCO group. So, the reaction was brought to room temperature after 2 h of reaction in the second step, in order to incorporate RCD and control the reaction without gel formation. RCD reacted with some of the hydroxyl-terminated pre-polymer chains and endows with strong interfacial interactions. The degree of interaction between the nanomaterial and the polymer depends on the level of RCD dispersion into the HPU matrix.

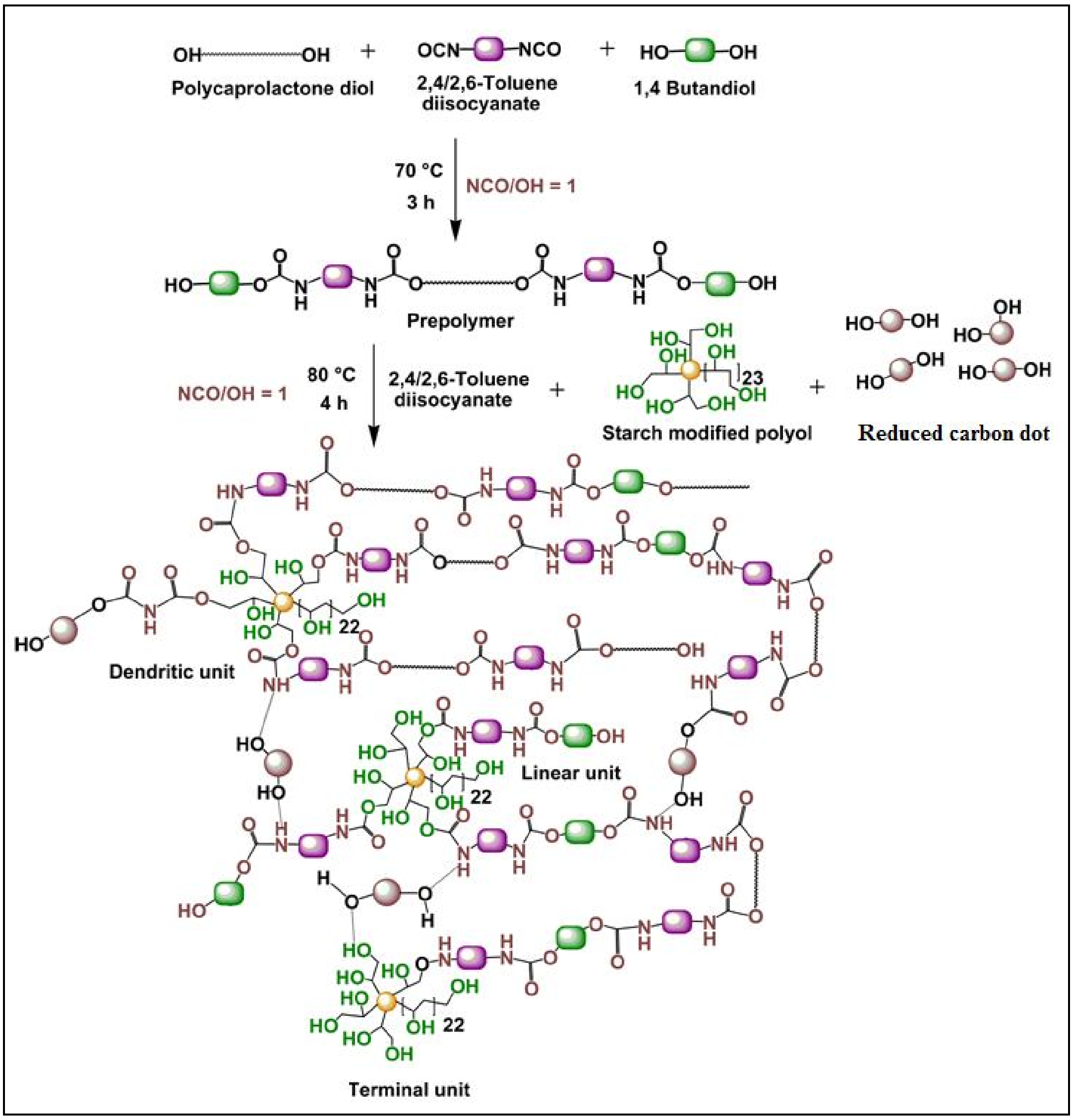

Scheme 4B.1. Fabrication of HPU/RCD nanocomposite.

The homogenous dispersion of the nanomaterial depends upon the nature of the polymer, technique of nanocomposite formation, the degree of modification, polar surface functionalities and primarily the compatibility between the nanomaterial and the polymeric matrix [12, 16]. Thus, the reaction temperature was gradually raised to (80 ± 2) °C and kept constant for another 2 h for completion of the reaction. The absence of band at 2270 cm^{-1} in the FTIR spectrum confirmed the absence of free -NCO group in the polymeric structure which validated the completion of the reaction. The completion of reaction was also further confirmed by the butyl amine test.

4B.3.2. Characterization of HPU nanocomposites

FTIR spectroscopic analyses showed the presence of different chemical functionalities in HPU and its nanocomposites as shown in **Figure 4B.1**.

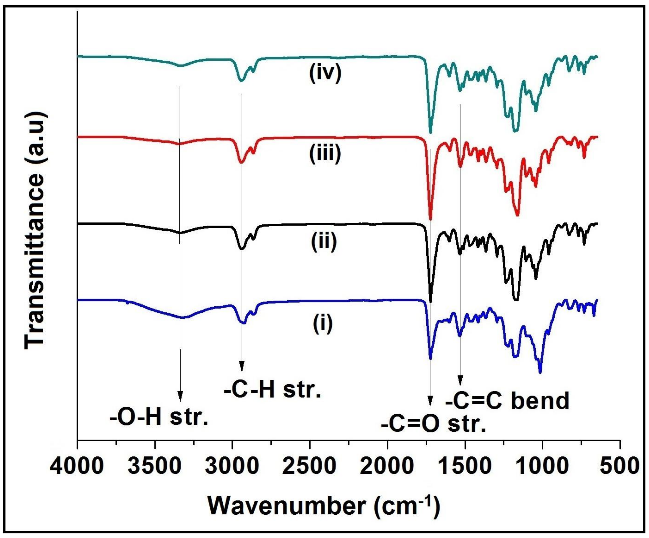

Figure 4B.1. FTIR spectra of (i) HPU, (ii) HPU/RCD0.5, (iii) HPU/RCD1 and (iv) HPU/RCD2.

The oxygeneous groups of RCD possess an intrinsic affinity to interact with HPU or its precursors by either non-covalently or covalently. From the FTIR spectrum of the nanocomposites, the absorption frequencies at 3463, 2974, 1726, 1600, 1527 and 1244 cm^{-1} confirmed the presence of -OH, -CH, -C=O, -C=C-, -NH and -CN overlap, and –C-O-C- groups, respectively [12, 16]. Such strong interfacial interactions play a vital role in the homogeneous distribution of the nanomaterial in the matrix [12]. In the XRD patterns, two separate peaks near $2\theta = 21°$ (d-spacing = 0.41 nm) and 23° (d-spacing =

0.375 nm) were observed due to the crystalline PCL moiety present in HPU as shown in **Figure 4B.2**. On incorporation of RCD, a shift in the PCL peaks was observed towards a higher angle. This may be attributed to the formation of an additional dense structure in comparison to the pristine HPU [23]. Also the increase in nanocomposite crystallinity with an increase in the nanomaterial dose indicates that the nanomaterial acts as a nucleating agent [24]. However, the XRD patterns of the nanocomposites showed no characteristic peak for RCD.

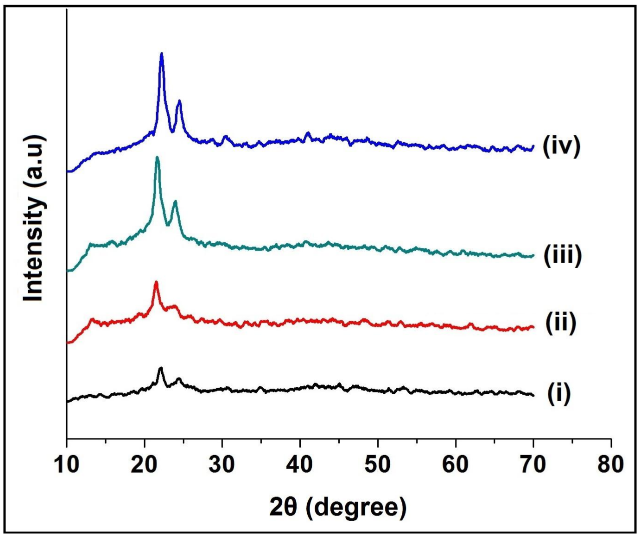

Figure 4B.2. XRD patterns of (i) HPU, (ii) HPU/RCD0.5, (iii) HPU/RCD1 and (iv) HPU/RCD2.

This may be attributed to the presence of a relatively small amount of RCD in the nanocomposites and chemical bond formation with HPU chains. The Raman spectrum of HPU/RCD in **Figure 4B.3** shows the D, G and 2D bands at 1350 cm^{-1}, 1603 cm^{-1} and 2723 cm^{-1}, respectively, similar to that of RCD. A noteworthy difference was the increase in the D band intensity in comparison to that of pristine RCD. This was attributed to the creation of further disorder in the structure of RCD during nanocomposite fabrication. This indicates definite interaction between RCD and HPU matrix [12].

The dispersion of the nanomaterial in the polymeric matrix strongly influences the material performance of the nanocomposites. From the TEM image of HPU/RCD2, it is clear that there is a uniform distribution of RCD in the HPU matrix even at the highest loading of nanomaterial (**Figure 4B.4a**).

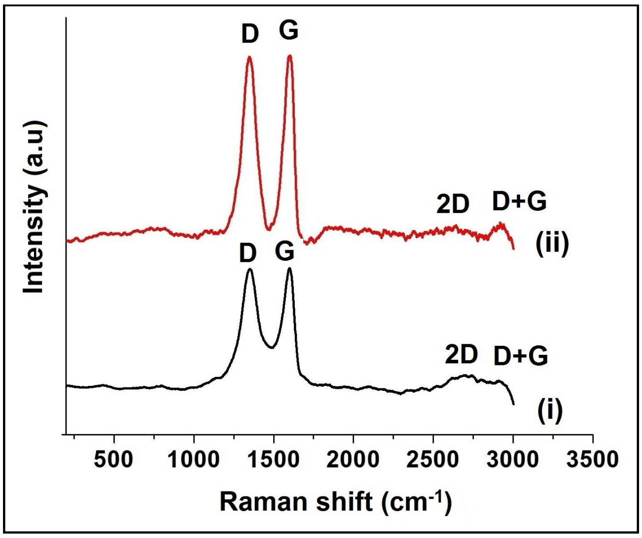

Figure 4B.3. Raman spectra of (i) RCD and (ii) HPU/RCD2.

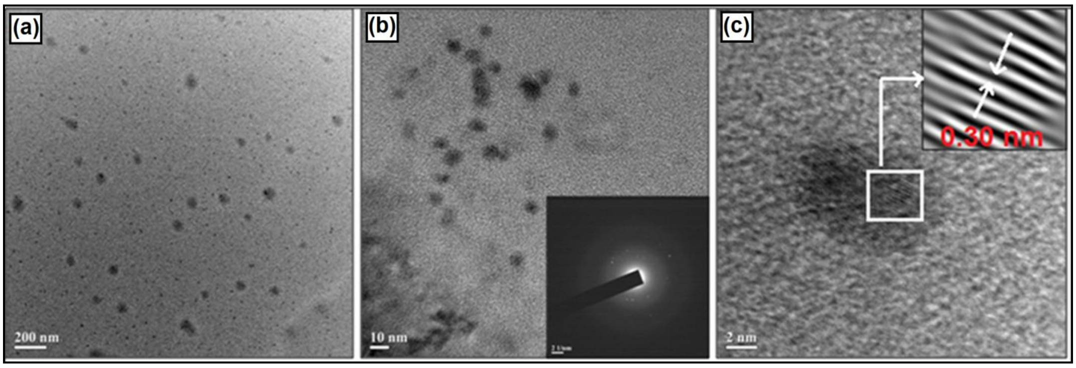

Figure 4B.4. TEM images of HPU/RCD2 at magnifications of **(a)** 100 nm, **(b)** 10 nm, SAED pattern of HPU/RCD2 as inset and, **(c)** 5 nm (IFFT image showing the lattice fringes as inset).

The enhancement of the amorphous nature of RCD in the nanocomposite was confirmed by SAED pattern (inset of **Figure 4B.4b**). HRTEM and IFFT images revealed that the inter-planar distance was 0.30 nm as observed from lattice fringe of RCD at the inset of **Figure 4B.4c**. The lattice spacing of RCD was increased after the fabrication of nanocomposite. This may be due to intercalation upon formation of the nanocomposite as RCD has layered graphitic structure. The incorporation of RCD in the fabrication reaction may additionally reduce the crystallinity of the already poorly crystalline RCD.

4B.3.3. Mechanical properties

Generally, suture applications demand high strength, toughness and flexibility of the final threads [7, 8]. Unfortunately pristine polymeric material alone cannot offer adequate strength and bioactivity as a suitable suture. Sutures with low tensile strength have a tendency to break during surgery, or more critically, post surgery. In the earlier case, the surgeon ought to spend more time and effort in re-suturing the wound whereas in the latter, loss of wound closure and infection may possibly occur [25]. A perceptible accomplishment of the present study is the concurrent enhancement of elongation at break and tensile strength, which effected in the elevated toughness of all the three compositions of the nanocomposites (**Table 4B.1**).

Table 4B.1. Mechanical properties of HPU and its nanocomposites

Property	HPU	HPU/RCD0.5	HPU/RCD1	HPU/RCD2
Tensile strength (MPa)	17.6 ± 0.5	20 ± 0.2	25.79 ± 0.3	32.14 ± 0.2
Elongation at break (%)	1158 ± 4	1284 ± 3	1420 ± 3	1576 ± 3
Hardness (Shore A)	40 ± 0.5	45 ± 0.3	46 ± 0.2	48 ± 0.3
Impact strength[a] (kJ m^{-1})	>19.02	>19.02	>19.02	>19.02
Toughness[b] (MJ m^{-3})	136.7 ± 3	189.8 ± 3	299.2 ± 3	439.2 ± 2

[a] *Maximum limit of the instrument.*

[b] *Calculated by integrating the area under stress-strain curves.*

This can be attributed to three primary factors, namely, (i) the fine dispersion of RCD in the matrix, without agglomeration; (ii) the advanced physico-chemical interactions of carbon rich graphitic structure of RCD with the HPU matrix by virtue of its optimum number of polar peripheral functional groups; and (iii) the good compatibility and strong interfacial adhesion between HPU and the carbon rich graphitic RCD. These contribute to the remarkable toughness of the nanocomposite [12]. These strong H-bonding, covalent bonding, and polar-polar interactions between RCD and the HPU chains stiffen the hard segments of HPU and assists in the successful load dissipation from the HPU matrix to the nanomaterial in the nanocomposite [12, 23, 26]. Thus, the tensile strength of the nanocomposites was greatly enhanced as shown in their stress-strain curves in **Figure 4B.5a**. The nanocomposites also confirmed an effective dose dependent toughness. HPU/RCD2 and HPU/RCD0.5 exhibited the highest and the lowest toughness, respectively as shown in **Figure 4B.5b**. Again, Gogoi *et al.* reported that there was a decrease in elongation at break by 44% after fabrication of the pristine waterborne PU with CD [12]. This might be attributed to the large number of polar functional groups which restricts the segmental motions of the polymer chains and diminish the elongation at break [12]. On the other hand, the overall elongation at break of HPU/RCD nanocomposites was found to be very good (**Table 4B.1**). The excellent compatibility of RCD with the HPU matrix serves as the proper alignment of the HPU chains during the preliminary stage of tensile loading and forces them to orient the multi layered graphitic structure (as evident by TEM infringes analysis in **Figure 4B.4**) in RCD along the direction of loading.

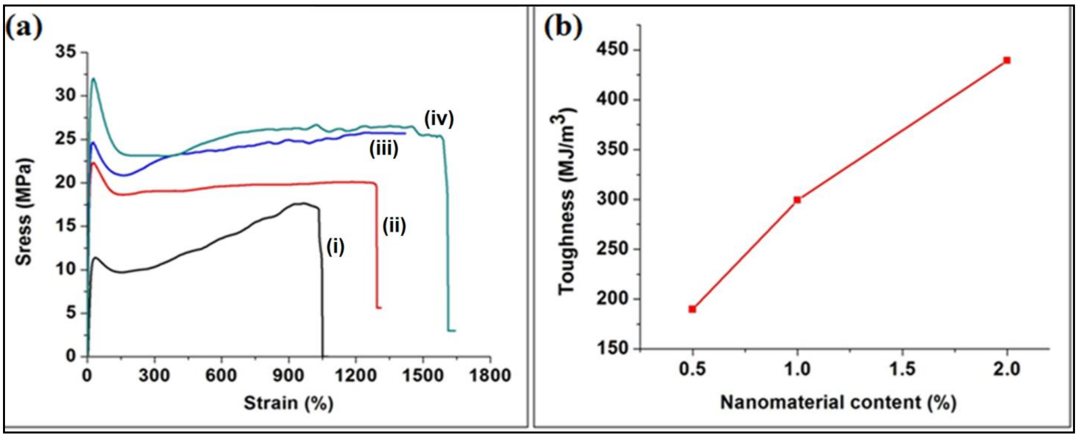

Figure 4B.5. (a) Stress-strain profiles of (i) HPU, (ii) HPU/RCD0.5, (iii) HPU/RCD1 and (iv) HPU/RCD2; and **(b)** Stress-strain profile of toughness of HPU/RCD2.

Upon application of a mechanical stress on the nanocomposites, alignment of HPU chains along the direction of loading during initial stress and sliding of the graphene layers over one another during high stress contributed to the improved elongation. Similar phenomenon was observed in RGO based polymeric system where both the strength and strain of the nanocomposites were enhanced owing to the same mechanism [23]. Thus, similar trend may arise in fabricated nanocomposites provided the nanomaterial can covalently link with the polymeric chain. The low hardness values of the nanocomposites indicate the suitability as a suture material which helps to prevent injury to the body tissues (**Table 4B.1**). Also, the HPU nanocomposites exhibited the maximum impact energy owing to the presence of soft segments in the HPU matrix that dissipates the impact energy [27]. Thus, overall mechanical performance of HPU/RCD2 was found to be adequate and hence found to be suitable for its application as a suture. However, the tensile strength (MPa) of commercially available suture is very high (ETHILON: 407.18, MAXON: 485.71, NOVAFIL: 405.40, Prolene: 420.2 and Duracryl: 444.26) though the elongation at break (%) is relatively low (ETHILON: 52.6, MAXON: 93.6, NOVAFIL: 76.2, Prolene: 63.8 and Duracryl: 95.6) [28]. It is pertinent to mention here that the tensile strengths of the commercial sutures were determined by twisting the drawn out fibers into a thread like structure which resulted in sufficiently high strength. The surface morphology of the fractured nanocomposite films are shown in **Figure 4B.6a** and **b** as the SEM images. The nanocomposite demonstrated a micro-rough fracture surface due to the deformation or the matrix shear yielding of the polymer with RCD. The alignment of the structural deformation of the nanocomposite along the same direction can also be seen from the SEM micrographs.

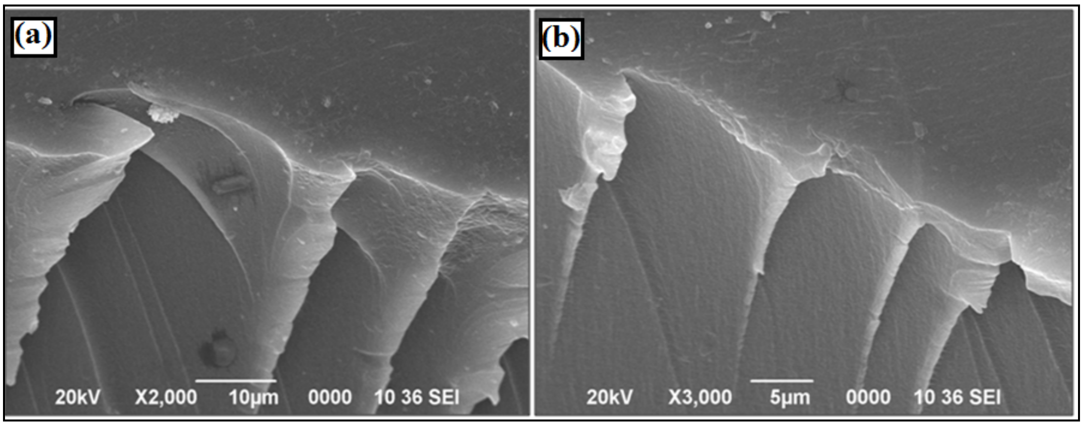

Figure 4B.6. SEM micrographs of the fractured surface of HPU/RCD2 at magnification **(a)** 10 µm and **(b)** 5 µm.

4B.3.4. Thermal properties

Thermal study of HPU nanocomposites was conducted to understand the degradation patterns of them. The nanocomposites exhibited a two-step degradation patterns due to the presence of both hard and soft segments in HPU matrix **(Figure 4B.7)**. This suggests that the nature and loading of the nanomaterial do not drastically control the degradation mechanism of the nanocomposites. All the nanocomposites exhibited particularly higher thermal stability as compared to HPU (**Table 4B.2**). The improved thermo-stability of the nanocomposites is attributed to the restricted motion of the HPU chains by the diverse physicochemical interactions, such as non-covalent and covalent interactions with RCD [12]. The nanomaterial in the polymeric matrix occupied the free space and contributed to the rigidity of the system. This resulted in the delay of the molecular thermal chain motion which enhances the thermal stability. Moreover, the restrictions imposed by RCD on the molecular chain mobility of HPU resulted in the improvement of T_m.

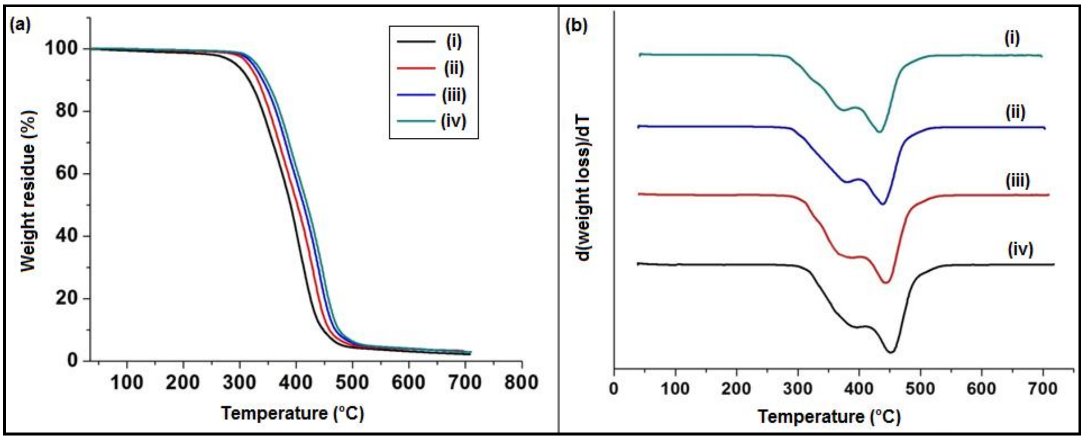

Figure 4B.7. (a) TGA thermograms and **(b)** DTG curves of (i) HPU, (ii) HPU/RCD0.5, (iii) HPU/RCD1 and (iv) HPU/RCD2.

Table 4B.2. Thermal properties of HPU and its nanocomposites

Parameter	**HPU**	**HPU/ RCD0.5**	**HPU/ RCD1**	**HPU/ RCD2**
Peak temperature for 1st stage degradation (°C)	371.2	378	382	388
Peak temperature for 2nd stage degradation (°C)	431.5	441.2	446.4	450.3
Weight residue (%)	2.7	3.2	3.4	3.7
Melting temperature (T_m,°C)	39.2	40.6	41.5	42.3
Melting enthalpy (J g^{-1})	43.4	44.3	46.5	47.6

The nanomaterial also effectively curbs the movement of the HPU chains. This clearly indicated that RCD served as the nucleating agent, and helped to improve the crystallization process by arrangement of the polymeric chains along a particular direction [12, 23].

On the other hand, melting temperature (T_m), melting enthalpy (ΔH_m) and crystallization behavior of HPU nanocomposites were found to increase with an increase in the nanomaterial content as given in **Table 4B.2**. It was observed that T_m of the soft segment was evidently reliant on the amount of RCD and shifted to higher temperature with the increase of the nanomaterial content (**Figure 4B.8**). The presence of nanomaterial provides restrictions on the molecular mobility of HPU chains and thereby enhancing the T_m of the nanocomposites [23]. Pokharel *et al.* confirmed comparable enhancement in T_m for graphene modified polymeric nanocomposite [29]. They reported that strong interaction between the polymer matrix and the nano-sheets as well as good dispersion leads to the arrangement of an inter-phase zone around each sheet where polymeric chain mobility is hampered. The enhancement of crystallinity can also be predicted from the ΔH_m values. The improvement of crystallinity of a semi crystalline polymer on incorporation of various nanomaterials has been reported in relevant literatures [12, 23, 30]. This clearly signifies that the homogenously distributed RCD provide as the nucleating agent and improves the crystallization process by arrangement of the soft segment along a particular direction [12, 31].

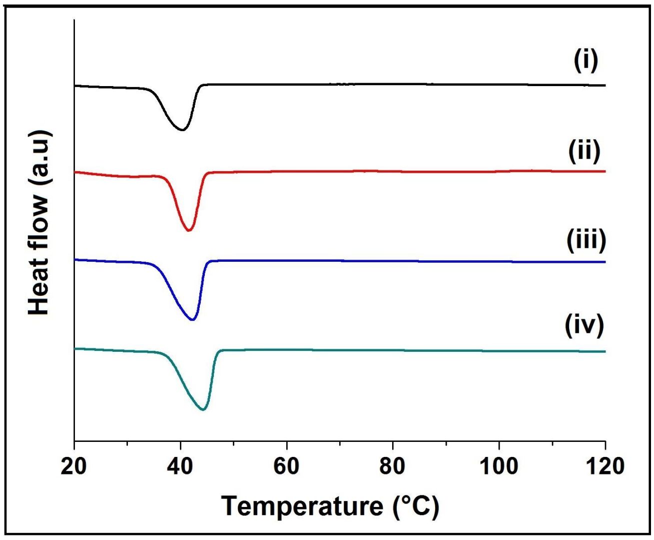

Figure 4B.8. DSC curves of (i) HPU, (ii) HPU/RCD0.5, (iii) HPU/RCD1 and (iv) HPU/RCD2.

4B.3.5. In vitro degradation study

The results of the *in vitro* degradation without any enzyme study showed mass loss from the films over the period of 90 days in PBS, where degradation has started from the surface, as shown in **Figure 4B.9**. Within the first 30 days, the control HPU film showed 1.4% mass loss. The nanocomposite HPU/RCD0.5 film showed higher mass loss (3%) as compared to the HPU film ($p \leq 0.05$). The HPU/RCD1 and HPU/RCD2 films did not show any significant difference with the HPU film. Post 60 days of incubation, the mass loss of HPU film increased to 2%, while the nanocomposite films showed much higher mass loss ($p \leq 0.01$). Among the nanocomposites HPU/RCD0.5 showed the highest mass loss of 4.5%. At the end of 90 days, a similar pattern was observed with the HPU film showing the least mass loss (3%) among the tested samples. The nanocomposite films showed significantly higher mass loss ($p \leq 0.01$), peaking at 7% in case of HPU/RCD0.5. Therefore, the addition of nanomaterial increased the degradability of the HPU film.

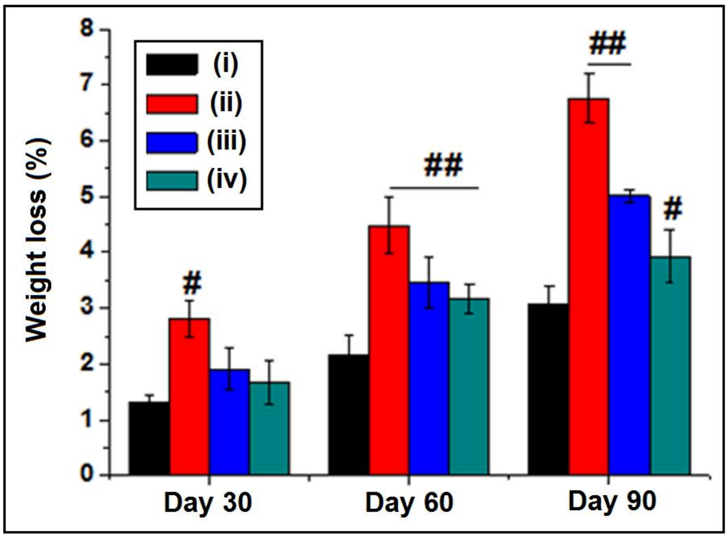

Figure 4B.9. *In vitro* degradation in PBS for 90 days of (i) HPU, (ii) HPU/RCD0.5, (iii) HPU/RCD1 and (iv) HPU/RCD2. Data are represented as mean ± SD (n = 3) ($^{\#}p \leq 0.05$ and $^{\#\#}p \leq 0.01$).

However, it is pertinent to note that the mass loss showed a gradient behavior with lower concentration of nanocomposite showing higher mass loss as compared to higher concentrations. A possible reason for this observation might be the secondary intra- and inter-molecular interactions between RCD and the HPU matrix. The results of our study were concurrent with a report by Das *et al.* [16], where with the use of nanocomposites in the polymer, the mass loss increased. Also, the results of our study were comparable with a earlier report by Sarkar *et al.* [32], where 13% *in vitro* degradation of PCL based polyurethane (PU) was observed in PBS medium after 8 weeks of exposure. Further, literature cites several reports on absorbable sutures with longer degradation rates (ranging from 180-210 days) such as MonoPlus (polydioxanone), Maxon (polyglyconate), Biosyn (glycomer 631), petcryl (polyglycolic acid), petcryl 910 (polyglactin 910), dexon (polyglycolic acid) sutures etc [33]. In most of the surgeries with deeper wound closure on the back or other high tension areas along with cartilage or tendon repair require effective wound support for longer duration of time. Thus, in such cases, sutures with low degradation rates and which do not dissolve even up to 90-120 days are suitable [34]. However, actual degradation of the suture primarily depends upon the body condition of the host. So depending upon the requirement, this suture needs to be tested for actual field application. Under *in vivo* study, the physiological condition in the host body will be different in the presence of different enzymes like proteases, lipases, amylases, etc. which accelerates the process of degradation. Thus, the present rates of degradation are suitable and it is expected that the sutures can degrade in a desired rate when implanted in the body of a host.

4B.3.6. Hemocompatibility assessment

Platelet adhesion is known to be a key mechanism that transduces the biomaterial thrombogenicity. One of the most important features of a suturing material is its anti-thrombogenic activity. Therefore, platelet adhesion and hemolysis assays were performed to assess hemocompatibility. Platelet adhesion was assessed by measuring the LDH activity which is a direct indication towards adhered activated platelets. The films containing nanocomposites showed significantly lower LDH activity as compared to the HPU film as shown in **Figure 4B.10a** ($p \leq 0.05$). No significant difference among the nanocomposite films was observed. The collagen coated surface used as positive control showed the highest LDH activity ($p \leq 0.01$). Therefore, the results show that the anti-thrombogenic activity of the HPU film was altered after nanocomposite formation. Compatibility of whole blood with the films and their interactions with RBC were analyzed by quantifying RBC lysis. The assay suggested minimal RBC lysis in the blood kept in contact with films containing nanocomposites as compared to unmodified HPU film as shown in **Figure 4B.10b** ($p \leq 0.01$). No significant difference was observed among the nanocomposite samples. All samples showed lower RBC lysis as compared to the positive control (20% TritonX-100) ($p \leq 0.01$).

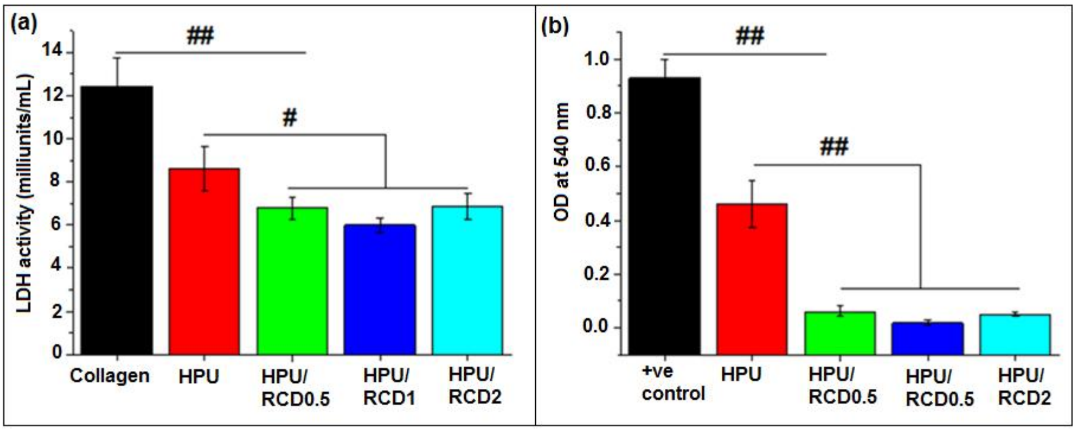

Figure 4B.10 (a) Quantification of platelet LDH activity and **(b)** hemolysis assay of HPU and its nanocomposites. Data are represented as mean ± SD (n = 3) ($^{\#}p \leq 0.05$ and $^{\#\#}p \leq 0.01$).

Results suggested improved anti-hemolytic activity and blood compatibility after nanocomposite incorporation in HPU matrix. Hence, these may be suitable candidate for developing sutures. The results were in concurrence with a previous report by Das *et al.*, showing the anti-hemolytic activity of nanocomposites composed of bio-based HPU [16].

4B.3.7. In vitro **immune response**

An ideal suture material for biomedical applications needs to be minimally immunogenic. Consequently, we studied mouse macrophage activity (in terms of TNF α release) in response to HPU/RCD nanocomposite films. Macrophages are the primary source of pro-inflammatory mediators like TNF-α which plays a crucial role in inflammation and regulation of the immune response. After 12 h of incubation, the macrophage seeded on films displayed significantly lower (~ 3-fold) secretion of TNF-α compared to those with LPS (positive control) ($p \leq 0.01$) as shown in **Figure 4B.11**. TNF-α production for the negative control TCP was significantly lower than all other samples ($p \leq 0.01$). No major difference was observed among the films. Therefore, the results indicate that the samples showed minimal immune response and were safe to be used as suturing material. Previous reports have shown nanocomposites of HPU to be biocompatible and non-immunological in behavior, indicating promising signs for the use of HPU based matrices as suture material along with other biomedical applications [12, 35].

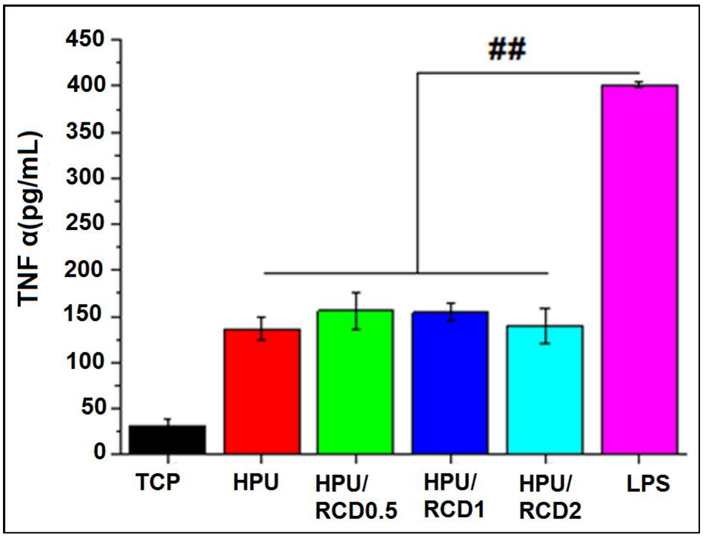

Figure 4B.11. ELISA-based determination of TNF-α release induced by HPU and its nanocomposites from RAW 264.7. Data are represented as mean ± SD (n = 3) ($^{\#}p \leq 0.05$ and $^{\#\#}p \leq 0.01$).

4B.3.8. In vitro cytocompatibility

SMC and EC are the major cell types of the blood vessels, hence it is appropriate to assess the biocompatibility of the material to these cells for their use as sutures in biomedical applications. Live cell imaging was performed to evaluate attachment and viability. As shown by the green stained regions of fluorescent microscopic images as shown in **Figure 4B.12a**, all the films showed viability for vascular cells which were uniformly distributed. Similarly, staining with Hoechst dye revealed homogenously distributed round healthy nucleus as shown in **Figure 4B.12b**. This endorses the suitable biocompatibility of the material for various biomedical applications including suturing material. Further, cell proliferation assay was carried out using Alamar Blue dye. The reduction of Alamar Balue directly relates to elevated cellular metabolism and proliferation. In case of SMC seeded nanocomposite, the results showed increased proliferation on films on day 7 as compared to day 1 as presented in **Figure 4B.12c** ($p \leq 0.01$). The proliferation of SMC on nanocomposite films was significantly higher than the HPU film and lower than the TCP after 7 days ($p \leq 0.01$). However, no significant difference in cellular proliferation was observed among the films. A similar trend was observed in case of EC seeded films, where the nanocomposite films like HPU/RCD0.5 and HPU/RCD2 showed significantly higher proliferation than HPU film and lower proliferation than HPU/RCD1 and TCP as shown in ($p \leq 0.01$). Therefore, the results indicate that incorporation of nanocomposite to the pristine HPU matrix enhances cellular proliferation. These results were in accordance with previous reports [36, 37].

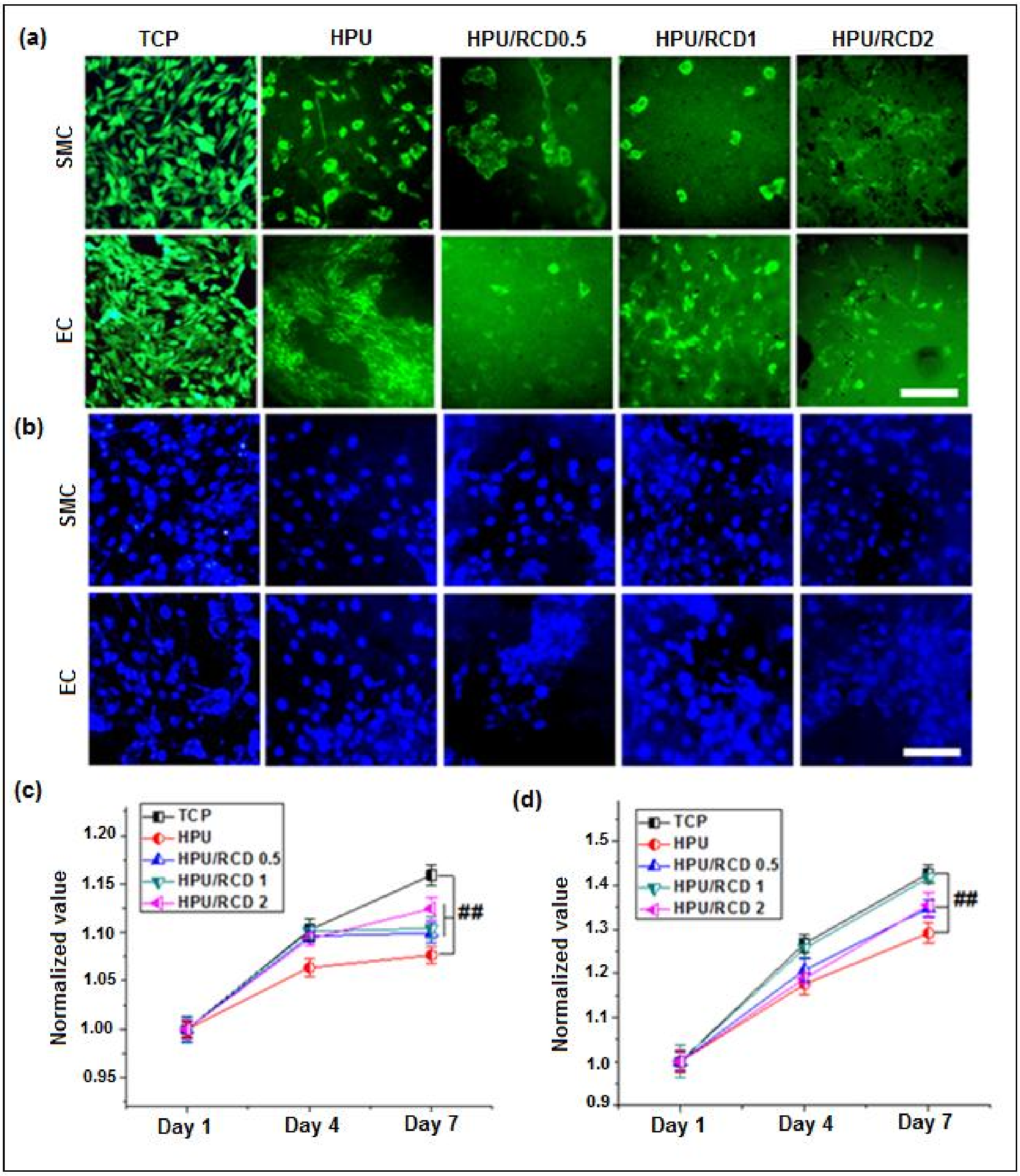

Figure 4B.12. (a) Images of live vascular cells (EC and SMC, green color) cultured on nanocomposite films. (Scale bar: 200 µm), **(b)** Hoechst 33342 staining of cell nucleus (blue color) representing the attachment of vascular cells on nanocomposite substrates. (Scale bar: 100 µm). Alamar Blue cell proliferation profile of **(c)** SMC and (d) EC. Data are represented as mean ± SD (n = 3) ($^{\#\#}p \leq 0.01$).

Further, literature cites that similar type of bio-based HPU matrix degrades into non-toxic and easily metabolized the products which are acceptable to the host body system [16]. Moreover, RCD is prepared from bio-based CD which have profound bio-activity (anti-oxidant behavior and hemocompatibility) and hence promote biocompatibility to the HPU nanocomposite system [12]. Reports have also demonstrated that TDI-based PU is non-toxic on the lungs isolated from guinea pigs and as a scaffold material had no toxic effect on Wistar rats [38, 39]. Also, no band corresponding to the aromatic toluene moiety was observed in the FTIR spectra, signifying that no such toxic fragments were leached out after degradation. Thus, the degraded products of HPU nanocomposite are non-toxic. Moreover, hemolytic assay of the degraded products and the leached out degraded by-products exhibited hemolytic activity of <5% as reported earlier [16]. However, to understand the toxic effect of such smart suture, animal study is essential before its actual field of applications.

4B.3.9. Smart suture self-tightening study

Self-tightening of suture is highly significant in its application as this property is challenging in endoscopic surgery to close an open lumen or an incision by tying the knot [2]. It is particularly complicated to control the suture in order that the wound lips are pressed jointly under the right stress. Thus, the potential resolution is the development of a self-tightening surgical suture where its temporary shape can be obtained by stretching the fibre by means of controlled stress. The self-tightening behavior of the suture is triggered by the human body temperature which leads to the shrinkage of the suture and subsequent tightening of the knot without any human intervention [9]. The thermal responsive shape memory behavior of HPU and its nanocomposites plays a role for self-tightening behavior as evaluated at (37 ± 1) °C and shown in **Figure 4B.13**. The shape memory effect of SMP can be considered as an entropic process [23, 24]. In the normal condition, the polymer stays in a permanent macroscopic form where the HPU polymeric chains are oriented in a random coil arrangement. Such state contributes to the highest entropy of the polymeric chains which leads to a stable state, thermodynamically. However, on heating the nanocomposite films at near ~ T_m + (20) °C, there is activation of chain mobility which help to stretch the films twice their original lengths.

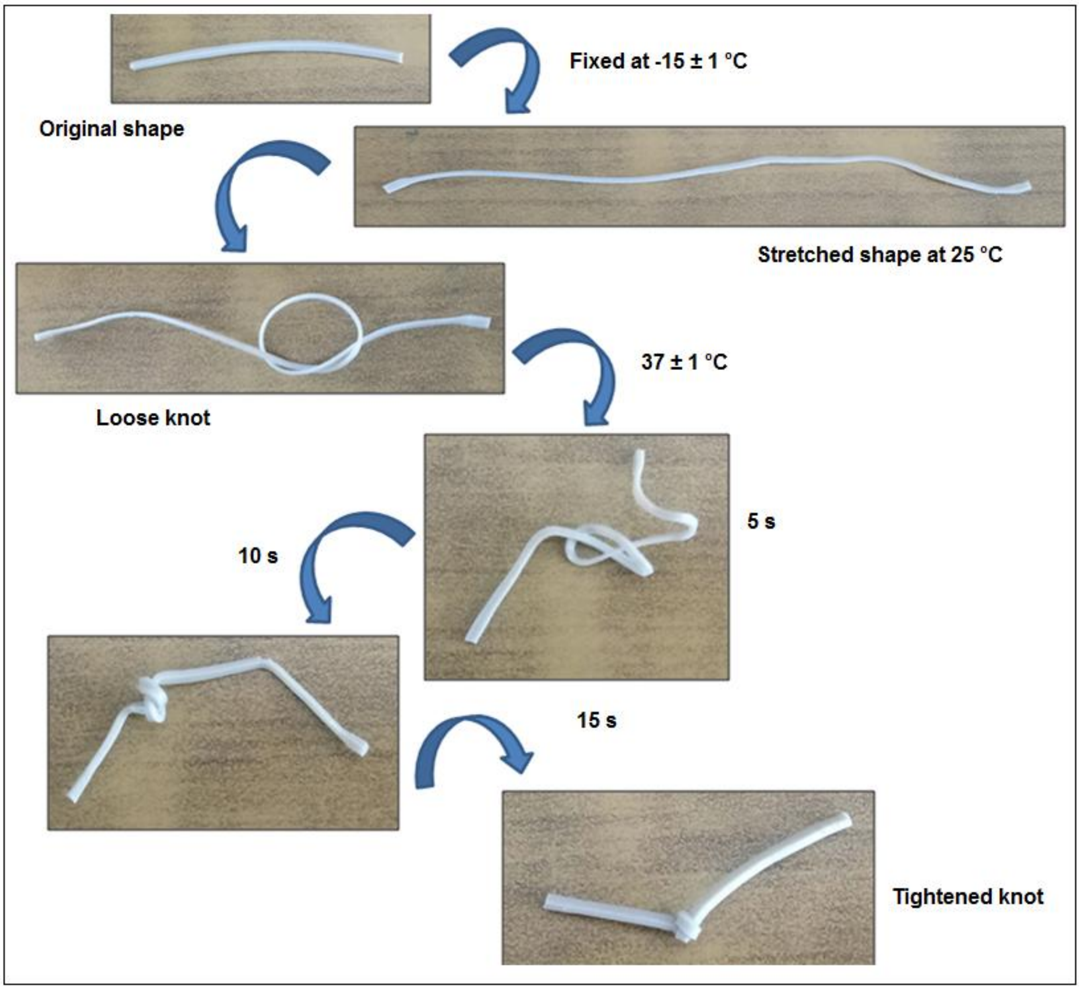

Figure 4B.13. Self-tightening behavior of HPU/RCD2.

Consequently, the fixing of temporary stretched shape of the film is due to the kinetic freezing of the HPU polymeric chains which is accompanied by lowering of their entropic state. This ultimately results in fixation of the temporary stretched shape. The polymeric chains did not have sufficient energy to revert back to its original shape, even after the mechanical force was removed. The film with the loose suture knot was then heated at (37 ± 1) °C, the molecular chain mobility was reactivated which permitted the polymeric chains return to the random coil motion after gaining of entropy [23, 40]. This led to the shrinking and tightening of the knot with optimum force. With increase in the wt% of RCD, the shape recovery of HPU nanocomposites was found to be significantly improved and HPU/RCD2 exhibited the highest shape recovery and the fastest self-tightening behavior (**Table 4B.3**). The shape recovery was found to be higher for the nanocomposite than most of the known SMP at body temperature [23, 24].

Table 4B.3. Shape memory properties of HPU nanocomposites

Property	HPU	HPU/RCD0.5	HPU/RCD1	HPU/RCD2
Shape recovery (%)	98.7 ± 0.1	99.3 ± 0.2	99.2 ± 0.1	99.7 ± 0.2
Shape fixity (%)	98.6 ± 0.1	99.1 ± 0.2	99.3 ± 0.3	99.6 ± 0.2
Shape recovery time (s)	20 ± 0.1	15 ± 0.1	15 ± 0.1	15 ± 0.1
Self-tightening time (s)	60 ± 2	25 ± 1	20 ± 1	15 ± 1

The improved shape recovery of the nanocomposites as compared to HPU is due to thermal conductivity of RCD, which aids in the efficient heating of the polymeric matrix, thus ensuing random orientation of the polymeric chains with the highest entropy [24].The homogeneous distribution of branching moiety, nanomaterial, hard segments and increased secondary interactions in the structure of HPU also contribute to the increased shape recovery by generation of strong net points [15]. Also RCD assist the nanocomposites to attain a high recovery stress attributed to the release of the stored elastic strain. The increase in shape recovery of HPU/RCD nanocomposites with increase in RCD wt% correlates the improved degree of crystallization to the growing development of shape recovery. The incorporation of RCD increased the crystallinity of the nanocomposites (as confirmed from DSC and XRD analyses). This effected in an augmented affinity for the production of large number of unlocked oriented chains. An immediate retractive stress is generated by these unlocked chains upon the elimination of load owing to elastic entropy which improves the shape recovery and decreases the self-tightening time of the nanocomposite. Therefore, a desired shape can be accomplished which can be sustained after cooling, by deforming such thermo responsive SMP. They can be utilized in the development of smart self-tightening suture for prospective minimally invasive endoscopic surgeries.

4B.4. Conclusion

The study established an innovative approach to obtain a tough, sustainable biodegradable rapid self-tightening polymeric suture material. Reduced carbon dot served as nano-reinforcing material to the fabricated starch modified hyperbranched polyurethane nanocomposite for the first time. The study witnessed enhanced mechanical and thermal properties as compared to the pristine hyperbranched polyurethane. Moreover, the fabricated nanocomposites exhibited excellent shape memory and self-tightening behavior within just 15 s at (37 ± 1) °C and were biodegradable. The assessment of hematological parameters confirmed the fabricated nanocomposite films to be hemocompatible. Additionally, cell proliferation and differentiation of SMC and EC revealed a cytocompatible material which corroborated its immense prospects in allied biomedical applications. The minimal *in vitro* immune response by the nanocomposites indicated its potential for future *in vivo* animal trials. Thus, the synchronized exhibition of such attractive characteristics by a single material substantiates the vision of utilizing the fabricated nanocomposites to develop rapid self-tightening polymeric sutures that could overcome the limitations associated with the generally used conventional sutures.

References

[1] Xie, T. Recent advances in polymer shape memory. *Polymer,* 52(22):4985-5000, 2011.

[2] Manavalan, R. A. and Mukhopadhyay, A. Surgical sutures: Performance, development and use. *Journal of Biomaterials and Tissue Engineering,* 1:1-36, 2009.

[3] Slade Shantz, J. A., Vernon, J., Morshed, S., Leiter, J., and Stranges, G. Sutures versus staples for wound closure in orthopaedic surgery: A pilot randomized controlled trial. *Patient Safety in Surgery,* 7(1):1-6, 2013.

[4] Paez, J., Martin, A., Sestafe, J., Jorge-Herrero, E., Millán, I., Navidad, R., Cordon, A., and Castillo-Olivares, J. Resistance and elasticity of the suture threads employed in cardiac bioprostheses. *Biomaterials,* 15(12):981-984, 1994.

[5] Reckhenrich, A. K., Kirsch, B. M., Wahl, E. A., Schenck, T. L., Rezaeian, F., Harder, Y., Foehr, P., Machens, H. G., and Egana, J. T. Surgical sutures filled with adipose-derived stem cells promote wound healing. *PloS One*, 9(3):e91169, 2014.

[6] Linberg, J. V., Mangano, L. M., and Odom, J. V. Comparison of nonabsorbable and absorbable sutures for use in oculoplastic surgery. *Ophthalmic Plastic & Reconstructive Surg*ery, 7(1):1-7, 1991.

[7] Pavan, A., Bosio, M., and Longo, T. A comparative study of poly- (glycolic acid) and catgut as suture materials. Histomorphology and mechanical properties. *Journal of Biomedical Materials Research Part B,* 13(3):477-96, 1979.

[8] Holmlund, E. W. Physical properties of surgical suture materials: Stress-strain relationship, stress-relaxation and irreversible elongation. *Annals of Surgery,* 184(2):189-193, 1976.

[9] Lendlein, A. and Langer, R. Biodegradable, elastic shape-memory polymers for potential biomedical applications. *Science,* 296(5573):1673-1676, 2002.

[10] Bennett, R. Selection of wound closure materials. *Journal of the American Academy of Dermatology*, 18(4)**:**619-637, 1988.

[11] Bichon, D., Borloz, W., and Cassaro-Zoppi, A. L. In vivo evaluation of a new polyurethane-coated catgut suture. *Biomaterials*, 5(5):255-263, 1984.

[12] Gogoi, S., Kumar, M., Mandal, B. B., and Karak, N. High performance luminescent thermosetting waterborne hyperbranched polyurethane/carbon quantum dot nanocomposite with in vitro cytocompatibility. *Composites Science and Technology,* 118:39-46, 2015.

[13] Lim, S. Y., Shen, W., and Gao, Z. Carbon quantum dots and their applications. *Chemical Society Reviews,* 44(1):362-381, 2015.

[14] Thakur, S. and N. Karak, Multi-stimuli responsive smart elastomeric hyperbranched polyurethane/reduced graphene oxide nanocomposites. *Journal of Materials Chemistry*, 2(36):14867-14875, 2014.

[15] ASTM F. 1635-04-Standart Test Method for in vitro Degradation Testing of Hydrolytically Degradable Polymer Resins and Fabricated Forms for Surgical Implants, ASTM International, Conshohocken, US, 2004.

[16] Das, B., Chattopadhyay, P., Mishra, D., Maiti, T. K., Maji, S., Narayan, R., and Karak, N. Nanocomposites of bio-based hyperbranched polyurethane/funtionalized MWCNT as non-immunogenic, osteoconductive, biodegradable and biocompatible scaffolds in bone tissue engineering. *Journal of Materials Chemistry B*, 1(33):4115-4126, 2013.

[17] Cutiongco, M. F., Anderson, D. E., Hinds, M. T., and Yim, E. K. *In vitro* and *ex vivo* hemocompatibility of off-the-shelf modified poly (vinyl alcohol) vascular grafts. *Acta biomaterialia*, 25:97-108, 2015.

[18] Gupta, P., Kumar, M., Bhardwaj, N., Kumar, J. P., Krishnamurthy, C., Nandi, S. K., and Mandal, B. B. Mimicking form and function of native small diameter

vascular conduits using mulberry and non-mulberry patterned silk films. *ACS Applied Materials & Interfaces*, 8(25):15874-15888, 2016.

[19] Singh, Y. P., Bhardwaj, N., and Mandal, B. B. Potential of agarose/silk fibroin blended hydrogel for in vitro cartilage tissue engineering. *ACS Applied Materials & Interfaces*, 8(33):21236-21249, 2016.

[20] Butcher, J. T. and Nerem, R. M. Porcine aortic valve interstitial cells in three-dimensional culture: comparison of phenotype with aortic smooth muscle cells. *The Journal of Heart Valve Disease,* 13(3):478-486, 2004.

[21] Singh, Y. P., Adhikary, M., Bhardwaj, N., Bhunia, B. K., and Mandal, B. B. Silk fiber reinforcement modulates in vitro chondrogenesis in 3D composite scaffolds. *Biomedical Materials*, 12(4):045012, 2017.

[22] Mandal, B. B. and Kundu, S. C. Cell proliferation and migration in silk fibroin 3D scaffolds. *Biomaterials,* 30(15):2956-2965, 2009.

[23] Thakur, S. and Karak, N. A tough smart elastomeric bio-based hyperbranched polyurethane nanocomposite. *New Journal of Chemistry,* 39(3):2146-2154, 2015.

[24] Thakur, S. and Karak, N. Bio-based tough hyperbranched polyurethane-graphene oxide nanocomposites as advanced shape memory materials. *RSC Advances,* 3(24):9476-9482, 2013.

[25] Hochberg, J., Meyer, K. M., and Marion, M. D. Suture choice and other methods of skin closure. *Surgical Clinics of North America,* 89(3):627-641, 2009.

[26] Pei, A., Malho, J. M., Ruokolainen, J., Zhou, Q., and Berglund, L. A. Strong nanocomposite reinforcement effects in polyurethane elastomer with low volume fraction of cellulose nanocrystals. *Macromolecules*, 44(11):4422-4427, 2011.

[27] Chen, D., Zhu, H., and Liu, T. In situ thermal preparation of polyimide nanocomposite films containing functionalized graphene sheets. *ACS Applied Materials & Interfaces*, 2(12):3702-3708, 2010.

[28] Naleway, S. E., Lear, W., Kruzic, J. J., and Maughan, C. B. Mechanical properties of suture materials in general and cutaneous surgery. *Journal of Biomedical Materials Research Part B,* 103(4):735-742, 2015.

[29] Pokharel, P., Pant, B., Pokhrel, K., Pant, H. R., Lim, J. G., Kim., H. Y., and Choi, S. Effects of functional groups on the graphene sheet for improving the thermomechanical properties of polyurethane nanocomposites. *Composites Part B: Engineering,* 78:192-201, 2015.

[30] Tzavalas, S., Mouzakis, D. E., Drakonakis, V., and Gregoriou, V. G. Polyethylene terephthalate multiwall nanotubes nanocomposites: Effect of nanotubes on the conformations, crystallinity and crystallization behavior of PET. *Journal of Polymer Science Part B,* 46(7):668-676, 2008.

[31] Gorbet, M. B. and Sefton, M. V. Biomaterial-associated thrombosis: roles of coagulation factors, complement, platelets and leukocytes. *Biomaterials,* 25(26)**:**5681-5703, 2004.

[32] Sarkar, D., Yailg, J. C., Sen, G. A., and Lopina, S. T. Synthesis and characterization of L-tyrosine based polyurethanes for biomaterial applications. *Journal of Biomedical Materials Research Part A,* 90(1):263-271, 2009.

[33] Chellamani, K. P., Veerasubramanian, D., and Balaji, R. V. Surgical sutures: An overview. *Journal of Academia and Industrial Research*, 1**:**778-782, 2013.

[34] Hayes, M. *Practical Skin Cancer Surgery.* Elsevier, Australia, 1st edition, 2014.

[35] Das, B., Mandal, M., Upadhyay, A., Chattopadhyay, P., and Karak, N. Bio-based hyperbranched polyurethane/Fe_3O_4 nanocomposites: smart antibacterial biomaterials for biomedical devices and implants. *Biomedical Materials,* 8(3):035003, 2013.

[36] Hsu, S. H., Tang, C. M., and Tseng, H. J. Biocompatibility of poly (ether) urethane-gold nanocomposites. *Journal of Biomedical Materials Research Part A,* 79A(4):759-770, 2006.

[37] Hung, H. S., Wu, C. C., Chien, S., and Hsu, S. H. The behavior of endothelial cells on polyurethane nanocomposites and the associated signaling pathways. *Biomaterials*, 30(8):1502-1511, 2009.

[38] Lastbom, L., Colmsjo, A., Johansson, R., Karlsson, D., Melin, J., Nordqvist, Y., and Skarping, G. Effects of thermal degradation products from PU foams based on toluene diisocyanate and diphenylmethane diisocyanate on isolated, perfused lung of guinea pig. *Scandinavian Journal of Work, Environment & Health,* 29(2):152-158, 2003.

[39] Cai, Y., Jiang, J. S., Zheng, B., and Xie, M. R. Synthesis and properties of magnetic sensitive shape memory Fe_3O_4/poly(ε-caprolactone)-polyurethane nanocomposites. *Journal of Applied Polymer Science,* 127(1)**:**49-56, 2013.

[40] Mya, K. Y., Gose, H. B., Pretsch, T., Bothe, M., and He, C. Star shaped POSS-polycaprolactone polyurethanes and their shape memory performance. *Journal of Materials Chemistry,* 21(13):4827-4836, 2011.